PHYSICAL REVIEW D **96,** 124005 (2017)

r-process nucleosynthesis from matter ejected in binary neutron star mergers

Luke Bovard,[1] Dirk Martin,[2,3] Federico Guercilena,[1] Almudena Arcones,[2,3] Luciano Rezzolla,[1,4] and Oleg Korobkin[5]

[1]*Institut für Theoretische Physik, Johann Wolfgang Goethe-Universität, Max-von-Laue-Straße 1, 60438 Frankfurt, Germany*

[2]*Institut für Kernphysik, Technische Universität Darmstadt, Schlossgartenstraße 9, 64289 Darmstadt, Germany*

[3]*GSI Helmholtzzentrum für Schwerionenforschung GmbH, Planckstrasse 1, Darmstadt 64291, Germany*

[4]*Frankfurt Institute for Advanced Studies, Ruth-Moufang-Straße 1, 60438 Frankfurt, Germany*

[5]*Center for Theoretical Astrophysics, Los Alamos National Laboratory, Los Alamos, New Mexico 87545, USA*

(Received 26 September 2017; published 5 December 2017)

When binary systems of neutron stars merge, a very small fraction of their rest mass is ejected, either dynamically or secularly. This material is neutron-rich and its nucleosynthesis provides the astrophysical site for the production of heavy elements in the Universe, together with a kilonova signal confirming neutron-star mergers as the origin of short gamma-ray bursts. We perform full general-relativistic simulations of binary neutron-star mergers employing three different nuclear-physics equations of state (EOSs), considering both equal- and unequal-mass configurations, and adopting a leakage scheme to account for neutrino radiative losses. Using a combination of techniques, we carry out an extensive and systematic study of the hydrodynamical, thermodynamical, and geometrical properties of the matter ejected dynamically, employing the `WinNet` nuclear-reaction network to recover the relative abundances of heavy elements produced by each configurations. Among the results obtained, three are particularly important. First, we find that, within the sample considered here, both the properties of the dynamical ejecta and the nucleosynthesis yields are robust against variations of the EOS and masses. Second, using a conservative but robust criterion for unbound matter, we find that the amount of ejected mass is $\lesssim 10^{-3}\ M_{\odot}$, hence at least one order of magnitude smaller than what normally assumed in modelling kilonova signals. Finally, using a simplified and gray-opacity model we assess the observability of the infrared kilonova emission finding, that for all binaries the luminosity peaks around $\sim 1/2$ day in the H-band, reaching a maximum magnitude of -13, and decreasing rapidly after one day.

DOI: 10.1103/PhysRevD.96.124005

I. INTRODUCTION

The recent detections of gravitational waves from binary neutron stars [1] (BNS) and binary black hole mergers [2–4] by the LIGO/Virgo Scientific Collaboration has signalled the beginning of the era of gravitational-wave astronomy and multimessenger astronomy. In the coming years, additional detectors such as KAGRA and the Einstein Telescope (ET) [5–7] are coming online or projected for operation and will allow for a new observational window on the Universe, complementary to the electromagnetic one.

The simultaneous detection of an electromagnetic counterpart [8,9] alongside GW170817 has provided convincings evidence that explains the long-standing puzzle of the origin of short gamma-ray bursts (SGRBs) in terms of merging BNSs [1,8,10–13]. Although only a single neutron star merger has so far been detected, more BNS mergers are expected to be observed in the coming years. Anticipating these observations, significant progress has been made over the last decade to accurately simulate their inspiral, merger and post-merger dynamics (see Refs. [14,15] for some recent reviews).

An electromagnetic counterpart from a merger that has recently received significant attention is that of a kilonova [16–31]. A kilonova is an infrared/optical signal powered by the decay of a variety of heavy elements, with a dominant contributions from the elements near the second *r*-process peak (i.e., ^{133}I, ^{132}Te and ^{133}Xe), and subdominant ones from the third *r*-process peak and unstable transuranian elements. Throughout the history of our Universe this process has given rise to about half of the elements heavier than iron. These elements can be formed after a BNS merger due to the onset of rapid neutron-capture process (*r*-process; see Ref. [32] for a recent review). Prior to the simultaneous detection of a kilonova with GW170817, kilonovae may have potentially already been observed in GRB 130603B [33,34], GRB 060614 [35,36] and GRB 050709 [37], but the very large uncertainties in these measurement have so far prevented an unambiguous identification.

While the fundamental concept of *r*-process has been known for decades [38], its astrophysical origin has not been unambiguously identified yet. For matter to undergo *r*-process nucleosynthesis, in fact, a very neutron-rich and

explosive environment is required and this puts constraints on the potential astrophysical sites where the process should take place. The two commonly suggested astrophysical sites are core-collapse supernovae and BNS mergers. Recent simulations of core-collapse supernovae (CCSN) have shown that the environment in the outer layers of the explosion is not neutron-rich enough and have been unable to reproduce the observed solar system abundances of heavy elements [39–42], although rare forms of CCSN driven by magnetic fields are also a possibility [43–45]. In contrast, neutron star mergers are considered an increasingly likely source of heavy elements. Recent observations of ultrafaint dwarf galaxies [46] have strongly pointed towards BNS mergers being the main site of production of *r*-process elements.

Furthermore, increasingly sophisticated numerical-relativity simulations with neutrino transport have shown that not only significant amounts of material are ejected (due to a variety of physical processes) in BNS mergers, but the environment in the ejecta provides the necessary conditions to trigger and sustain robust *r*-process nucleosynthesis. Numerous simulations ranging from Newtonian to full relativistic, with a variety of microphysical treatments, have shown four broad ejection mechanisms. These are: dynamical ejecta [21,23,24,26,47–56], neutrino-driven winds [20,22,25,57–61], magnetically driven winds [62–66], and viscous evolution of the accretion disk [67–70]. Their typical time scales are approximately $\sim$10 ms for dynamical ejecta, $\sim$100 ms for magnetically driven or neutrino-driven winds, and $\sim$1 s for viscous evolution. Due to the high computational cost of performing long-term fully relativistic simulations, mostly dynamical ejecta have been studied in full relativity, while other mechanisms have been the subject of mostly Newtonian simulations.

In this work, we present a number of high-resolution numerical-relativity simulations of BNS mergers to investigate the effects of the neutron-star initial masses, mass ratios and most importantly the microphysical equation of state (EOS) on the resulting *r*-process nucleosynthesis. We consider three fully temperature-dependent EOSs spanning a wide range of stiffness as measured from the stellar compactness, i.e., the ratio of the mass and radius of the corresponding nonrotating models. For each EOS, we consider three equal-mass initial setups covering a realistic range of initial BNS masses. Additionally, we consider for each EOS one unequal-mass case.

To follow the evolution of the fluid, we use a combination of techniques, namely outflow detectors and passively advected fluid tracers. The properties and use of the latter in general-relativistic simulations have been discussed in Ref. [71]. We then post-process the data using a complete nuclear-reaction network [43,72] to obtain the final *r*-process abundances. We also compute the associated kilonova light curves using the model outlined in Ref. [19].

We find that the amount of dynamically ejected mass is of the order of $10^{-3}\ M_\odot$, which, although rather small, is consistent with current constraints on the typical BNS merger rates and observed abundances of heavy elements in the Milky Way. Although some variation in the properties of the ejected mass (i.e., typical values of the electron fraction, entropy or velocity) are observed and appear to correlate with the choice of EOS or neutron-star mass for a given BNS model, these differences have minimal influence on the final *r*-process nucleosynthesis yields. Given the kilonova light curves associated to our simulations, we find that the prospects for their direct observation are rather limited; however, in view of the approximations made in our current analysis, this may be not a conclusive statement. Finally, we have uncovered an interesting geometrical structure in the angular distribution of the ejecta which could have important implications on the properties of the kilonova signal.

The paper is structured as follows: in Sec. II, we introduce the mathematical and numerical methods employed, together with the initial BNS configurations that we evolve. Section III, instead, summarizes the main properties of the physical models and numerical techniques that we employ to study the BNS evolution as well as to recover the heavy-element abundances. Sections IV–V D present our results and findings in terms of the mass ejected, the electron fraction, the specific entropy, and the ejecta velocity. Similarly, Secs. VII–VII B report our estimates for the kilonova light curves and their detectability, together with the constraints on the merger rates of BNSs. Finally, we conclude in Sec. IX.

Unless otherwise specified, we use a system of units such that $c = G = M_\odot = 1$, where c is the speed of light in vacuum, G is the gravitational constant, and $M_\odot$ is the mass of the Sun. We use Einstein's convention of summation over repeated indices. Latin indices run over 1,2,3, while Greek indices run over 0,1,2,3. The spacetime metric signature we adopt is $(-,+,+,+)$.

II. PHYSICAL SETUP AND INITIAL DATA

We consider both equal- and unequal-mass BNS systems on quasicircular orbits, with initial configurations constructed from three different EOSs, spanning a wide range in stiffness. From the stiffest to the softest, these EOSs are (i) DD2 [73]; (ii) LS220 [74] with compressibility parameter $K = 220$ MeV; SFHO [75]. Note that recent calculations in Ref. [76] have shown that the LS220 EOS does not satisfy constraints stemming from a lower bound on the energy per nucleon provided by the unitary-gas approximation. This result disfavors the LS220 as a viable model for the microphysics of neutron stars, but since this EOS is also one of the most well-studied in numerical applications, we include it in our study since it provides a useful comparison with the literature. Additionally, the DD2 and SFHO EOSs include additional light nuclei that are

TABLE I. Summary of the properties of the systems under consideration. The columns denote, respectively: the EOS; the gravitational mass ratio $q := M_1/M_2$ at infinite separation; the gravitational masses $M_{1,2}$ of the two stars at infinite separation; the stars' radii $R_{1,2}$ at infinite separation; the ADM mass $M_{\rm ADM}$ of the system; the baryon masses $M_{\rm b,1,2}$; the maximum mass of a nonrotating model of the given EOS $M_{\rm TOV}$; the radius of the maximum mass nonrotating model of the given EOS $R_{\rm TOV}$; the compactnesses $\mathcal{C}_{1,2} := M_{1,2}/R_{1,2}$; the total angular momentum J at the initial separation.

Model	EOS	q	M_1 $[M_\odot]$	M_2 $[M_\odot]$	R_1 [km]	R_2 [km]	$M_{\rm ADM}$ $[M_\odot]$	$M_{\rm b,1}$ $[M_\odot]$	$M_{\rm b,2}$ $[M_\odot]$	$M_{\rm TOV}$ $[M_\odot]$	$R_{\rm TOV}$ [km]	$\mathcal{C}_1$ -	$\mathcal{C}_2$ -	J $[M_\odot^2]$
DD2-M1.25	DD2	1.0	1.25	1.25	13.20	13.20	2.48	1.35	1.35	2.42	11.90	0.140	0.140	6.40
DD2-M1.35	DD2	1.0	1.35	1.35	13.23	13.23	2.68	1.47	1.47	2.42	11.90	0.151	0.151	7.31
DD2-M1.45	DD2	1.0	1.45	1.45	13.25	13.25	2.87	1.59	1.59	2.42	11.90	0.161	0.161	8.19
DD2-q09	DD2	0.9	1.22	1.35	13.19	13.23	2.55	1.31	1.47	2.42	11.90	0.136	0.151	6.68
LS220-M1.25	LS220	1.0	1.25	1.25	12.80	12.80	2.48	1.36	1.36	2.04	10.65	0.144	0.144	6.42
LS220-M1.35	LS220	1.0	1.35	1.35	12.75	12.75	2.67	1.47	1.47	2.04	10.65	0.156	0.156	7.26
LS220-M1.45	LS220	1.0	1.45	1.45	12.67	12.67	2.87	1.60	1.60	2.04	10.65	0.169	0.169	8.20
LS220-q09	LS220	0.9	1.21	1.35	12.81	12.75	2.61	1.32	1.47	2.04	10.65	0.140	0.156	6.98
SFHO-M1.25	SFHO	1.0	1.25	1.25	11.97	11.97	2.48	1.36	1.36	2.06	10.31	0.155	0.155	6.40
SFHO-M1.35	SFHO	1.0	1.35	1.35	11.92	11.92	2.68	1.48	1.48	2.06	10.31	0.167	0.167	7.28
SFHO-M1.45	SFHO	1.0	1.45	1.45	11.87	11.87	2.87	1.61	1.61	2.06	10.31	0.181	0.181	8.20
SFHO-q09	SFHO	0.9	1.22	1.35	11.97	11.92	2.55	1.32	1.48	2.06	10.31	0.150	0.167	6.67

not included in the LS220 and these change the neutrino interactions [77].

For each EOS, we consider three different equal-mass setups, with neutron-star gravitational masses of 1.25,1.35 and 1.45 $M_\odot$, respectively; and one unequal-mass system, with star masses of 1.2 and 1.35 $M_\odot$, resulting in a mass ratio $q = 0.9$ and a total ADM mass (see Ref. [78] for a definition) of the system which is intermediate between the two lightest equal-mass configurations for the same EOS. The stars' initial separation is chosen to be 45 km, resulting in an inspiral phase of approximately ∼3 orbits. Table I summarizes the properties of each system. The stars initial states are computed at neutrinoless beta equilibrium, i.e., at zero neutrino chemical potential, thus setting the initial values of the electron fraction. The initial data for every binary was constructed using the LORENE pseudospectral elliptic solver [79] and refers to irrotational binaries in quasicircular orbit.

III. METHODS

We summarize in this section the salient features of the physical models we employ to study the evolution of the BNS systems introduced in the previous section, as well as the numerical methods used and their implementation. In the interest of brevity, and since our approach does not significantly differ from well-known ones already described in the literature, we provide here only a succinct discussion.

A. General-relativistic hydrodynamics and neutrino transport

We model the neutron-star matter (as well as the matter ejected by the system) as a perfect fluid, using the temperature-dependent EOSs mentioned in the previous section.[1] The fluid evolution is described by the continuity equation, which expresses the conservation of baryon mass, and the relativistic Euler equations (taking the form of local conservation of the fluid stress-energy tensor components) (see Ref. [80] for a comprehensive discussion).

We include the contribution from neutrino interactions, which can change the composition of the material, and in particular the value of the electron fraction, which would be otherwise simply advected by the fluid velocity. To this end we employ a "leakage" scheme [81–83], which takes into account cooling due to neutrino emission, but does not model absorption and heating. In the presence of such interactions, a source term must be added both to the continuity equation and Euler equations, which, following [84], take the form

$$\nabla_\alpha(n_{\rm b}u^\alpha) = 0, \tag{1}$$

$$\nabla_\alpha(n_{\rm e}u^\alpha) = R, \tag{2}$$

$$\nabla_\beta T^{\alpha\beta} = Qu^\alpha, \tag{3}$$

where $n_{\rm b}$ and $n_{\rm e}$ are the baryon and electron number density, u^α is the fluid 4-velocity and $T^{\alpha\beta}$ is the fluid stress-energy tensor. Here, R is the net lepton-number emission rate, while Q is the net neutrino-cooling rate, and both are defined per unit volume and in the fluid rest-frame. A detailed discussion on the estimation of Q and R is contained in Refs. [24,84].

[1]Note that the use of a simple barotropic EOS would not be suitable here, since it would not capture the nonisentropic processes taking place after the merger and because neutrino interactions depend sensitively on the temperature and composition of the fluid.

The numerical scheme used to solve the hydrodynamics evolution equations is a finite-volumes method, applied to the flux-conservative formulation of Eq. (3). We employ the fifth-order MP5 [85] reconstruction operator, the HLLE Riemann solver [86] and the positivity-preserving limiter of Ref. [87,88]. We also make use of the refluxing technique [89] to minimize numerical spurious losses or gains of mass at the interface between refinement levels. The scheme is implemented in the WhiskyTHC code [88,90].

To integrate Einstein equations and obtain the spacetime evolution we use a fourth order finite-differences method applied to the BSSNOK formulation [91–93] of Einstein equations. The gauge conditions are the standard "1 + log" and "Gamma driver" choices (see, e.g., Ref. [94]). The spacetime evolution is provided by the McLachlan code [95], and coupled to the hydrodynamics evolution through the evaluation of the fluid stress-energy tensor.

An adaptive mesh refinement (AMR) approach based on the Carpet mesh-refinement driver [96] is used to increase resolution as well as extend the spatial domain, placing the outer boundary as close as possible to the wave zone. In particular, we employ a Cartesian 3D grid with six box-in-box levels of mesh refinement (promoted to seven after merger), so that the finest, innermost grid during the inspiral has a resolution of $0.15\ M_\odot \simeq 215$ m. The outer boundary of the domain extends to $512\ M_\odot \simeq 760$ km. The time step is fixed to one sixth of the grid spacing and a third-order strong stability preserving Runge-Kutta method is used for advancing the computation in time.

B. Tracer particles and outflow detectors

To follow the flow of ejected material we employ two different techniques. The first technique is the use of tracer particles [21,71,97,98], i.e., massless particles passively advected with the fluid. A total of 2×10^5 tracers are placed with a uniform distribution in the density interval $10^7\ \mathrm{g/cm^3} \lesssim \rho \lesssim 10^{15}\ \mathrm{g/cm^3}$ at the time of merger (see Ref. [71] for a discussion on why this distribution of tracers is the optimal one). Fluid properties are interpolated at the tracers location, providing a detailed account of the evolution of the associated fluid element. Following the description in Ref. [71], a "tracer mass" can be associated to the otherwise massless tracers by locally integrating a mass flux through a sphere of given radius. Combining this mass with the history of the evolution of the tracer particle provides the initial input for the nuclear-reaction network discussed in Sec. III D.

The second technique employed to follow the ejected material is the use of so-called outflow detectors, i.e., spherical surfaces placed at a fixed coordinate radius around the center of the computational domain. These detectors are able to measure the flux of the fluid through their surface and record the various hydrodynamical and thermodynamical quantities as a function of time. In our simulations, we employ nine detectors set at radii between 100 and $500\ M_\odot$ with a separation of $50\ M_\odot$. Each detector has a resolution of 55 points in the polar and 96 points in the azimuthal direction, and the detector located at a radius of $200\ M_\odot \approx 300$ km is our fiducial one. As the fluid passes through a detector spherical surface, hydrodynamical and thermodynamical variables are interpolated onto it, allowing us to record the entire evolution of the fluid in all angular directions. Note that we define the total ejected mass by integrating the unbound mass flux over the surface of the detector, in contrast to, e.g., Ref. [54], where the rest-mass density of all unbound fluid elements is integrated over the whole computational domain (see Sec. V A for further details).

C. Selection of unbound material

Regardless of whether tracer particles or outflow detectors are used, it is necessary to define a criterion to identify gravitationally unbound material, which will not accrete back onto the merger remnant and can be considered ejected from the system.

The difficulty in determining gravitationally unbound material arises mostly due to the finite size of the grid. Ejecta can only be followed to the edge of the computational domain, which is still relatively close to the BNS merger product, and can still be influenced by its gravitational potential. This problem could be alleviated by using a larger grid, but this comes at greater computational cost and a few numerical drawbacks (e.g., poor resolution in an AMR grid). Likewise, we are interested in tracking the evolution of the ejected material to study the kilonova signal, which is expected to peak days after merger. However, computing the evolution of the ejecta for such long timescales is currently computationally unfeasible in full numerical-relativity simulations, which can run at most for timescales on the order of tens of milliseconds after merger.

As such, a criterion to define unbound material is therefore needed and we choose to define a fluid element as "unbound" if it satisfies the so-called *geodesic criterion* (e.g., Refs. [23,99]), i.e., if $u_t \leq -1$, where u_t is the covariant time component of the fluid element 4-velocity. The justification of such a criterion is clear when considering its Newtonian limit. In this case $u_t \approx -1 - \phi - v^2/2$, where ϕ is the gravitational potential (see Ref. [80]). At large separations from the gravitational sources, the gravitational potential can be neglected, $\phi \simeq 0$ and thus $u_t \approx -1 - v^2/2 \leq -1$. The criterion amounts therefore to imposing that the fluid element should have non-zero velocity at infinity.

An alternative criterion that has been studied [99] is the so-called *Bernoulli criterion*. In this case, a fluid element is defined to be unbound if $hu_t \leq -1$, h being the fluid specific enthalpy. In the following, we only consider the geodesic criterion, and hereafter the adjective "unbound" will refer exclusively to material satisfying it. We consider

however the impact that the choice of the criterion for material to be unbound can have on the properties of dynamically ejected material in Appendix A, where we present a comparison of the results obtained with the geodesic and Bernoulli criteria. However, since $h \geq 1$ [80], it is clear that the Bernoulli criterion will be in general less restrictive than the geodesic one, yielding an amount of ejected material that is at least twice larger.

D. Nuclear network overview

The nucleosynthesis calculations are carried out with the complete WinNet nuclear-reaction network [43,72]. Over 5800 nuclei between the valley of stability and the neutron-drip line are taken into account. The reaction rates are taken from the compilation of Ref. [100] for the finite range droplet model (FRDM [101]) and we consider weak-interaction rates including neutrino absorption on nucleons [102,103]. Neutron-capture rates for nuclei with atomic number $Z \gtrsim 80$ and neutron-induced fission rates are taken from Ref. [104]. Moreover, we include beta-delayed fission probabilities from Ref. [105]. Our network has been used as a benchmark in a recent comparison with another general-purpose nuclear-reaction network [106], showing a very good overall agreement.

As detailed in Sec. VI, we post-process representative subsets of unbound tracers from the hydrodynamical simulations according to three different methods of selection. From every tracer, a time series of the rest-mass density, temperature, specific entropy, and electron fraction is extracted, on which the nuclear network acts. For each of these tracers, we start our calculations when the temperature drops below $T = 10^{10}$ K $= 10$ GK. Due to the high temperatures, the initial composition is given by nuclear statistical equilibrium (NSE), and is dominated by nucleons and alpha particles. We assume NSE to hold for $T \gtrsim 8$ GK. When the temperature drops below the NSE threshold, the composition is evolved with the full reaction network. As most of the tracer trajectories were simulated only until ~20 ms after the merger, we extrapolate them to very large distances using the following prescriptions for the position, density and temperature evolution [72,107]

$$r(t) = r_0 + v_0 t, \tag{4}$$

$$\rho(t) = \rho_0 \left(\frac{t}{t_0}\right)^{-3}, \tag{5}$$

$$T(t) = T[s, \rho(t), Y_e(t)]. \tag{6}$$

where ρ is the total rest-mass density, r the coordinate radius, v the 3-velocity, s the specific entropy, and $Y_e := n_e/n_b$ the electron fraction. The subscript "0" indicates the last available values from the hydrodynamical simulations, and the temperature is computed from the Helmholtz EOS [108,109]. This ansatz for the ejecta expansion is well justified, at least at late times, as shown in Ref. [71], where tracers were reported to move ballistically along radial directions and to expand adiabatically at large distances from the merger product.

Furthermore, we compute the energy released by the r-process and include its impact on the evolution of the fluid entropy [110]. In particular, the major contribution to the radioactive heating is expected to come from beta decays and we assume the energy to be about equally distributed between thermalizing electrons and photons, and escaping neutrinos and photons [111].

IV. OVERVIEW OF SIMULATIONS

In what follows we discuss the results from the simulations comparing the outflow properties of the dynamically ejected material such as: the mass ejected M_{ej}, the electron fraction Y_e, the specific entropy s, and the ejecta velocity v_{ej}, for the different simulation parameters.

To investigate the effects of the EOS and initial masses on the dynamical ejecta, and hence the r-process nucleosynthesis, a total of 12 simulations were run. To study the effects of the EOS, three fully temperature-dependent EOSs were used, spanning a wide range in stiffness. For each EOS, four different masses parameters were run with 3 equal-mass and 1 unequal-mass case. For each simulation, at least 10 ms after merger was simulated to ensure a sufficient time for the dynamical ejecta to reach 300 km, which is where the properties of the dynamical ejecta are measured.

For each BNS model, we simulate approximately ~3 orbits before merger and we define the time of merger to be the time at which the gravitational-wave amplitude reaches its first peak [112]; in the following we define the time origin such that $t = 0$ corresponds to the time of merger. Given the maximum mass of nonrotating neutron star models, M_{TOV}, and the initial mass of the merging binaries, all the mergers that do not yield a prompt collapse to a black hole produce a hypermassive neutron star (HMNS), i.e., a neutron star whose mass exceeds the maximum mass supported by uniform rotation, $M_{max} \simeq 1.20 M_{TOV}$ [113], and that is in a metastable equilibrium state supported by differential rotation, with a quasiuniversal rotation profile [114].

The three binaries which instead collapse to a black hole are `SFHO-M1.35`, `SFHO-M1.45`, and `LS220-M1.45` with the latter two being a prompt collapse. More specifically, for `SFHO-M1.45` the collapse is right at merger and results in very little material being ejected (see discussion in Sec. V A), while for `LS220-M1.45` the collapse takes place about ~0.5 ms after merger, which is sufficient to allow for material to be ejected. Finally for `SFHO-M1.35`, the collapses to a black hole takes place at ~10 ms after the merger, when the HMNS has lost sufficient angular momentum.

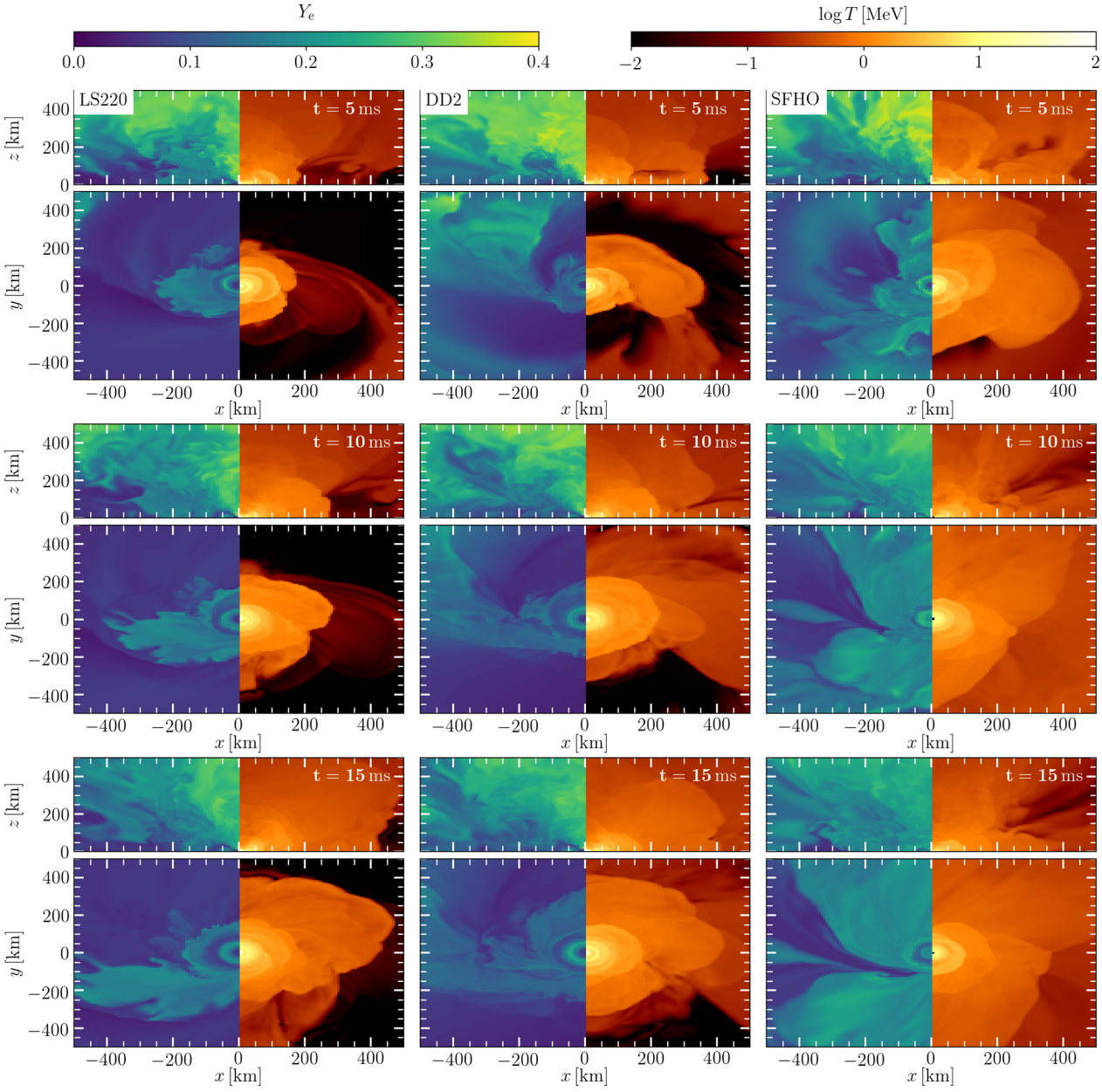

FIG. 1. Evolution of the electron fraction (left parts of panels) and of the temperature (right parts of panels) on the (x, z) plane (top panels) and on the (x, y) plane (bottom panels), for the different EOSs, namely: DD2, LS220, SFHO, from left to right. All panels refer to binaries with masses of $2 \times 1.35\ M_\odot$ and at the same representative times: 5 ms (top row), 10 ms (middle row), and 15 ms (bottom row) after the merger.

To show the spatial distributions of various quantities in the simulations, Fig. 1 reports three different time slices, 5, 10, 15 ms from top to bottom, of the electron fraction (left panels) and the temperature (right panels) in the (x, y)-(bottom panels) and (x, z)-planes (top panels) for the three different EOSs of $1.35\ M_\odot$ equal-mass initial data.

As anticipated in the Introduction, in terms of dynamical ejecta, there are two main processes which can eject material: tidal forces and shock heating. Tidal forces arise from tidal interactions during merging and eject material primarily along the orbital plane and are a manifestation of gravitational interactions. In comparison, shock heating, is approximately spherically symmetric [23] and depends on the thermal properties of the fluid. These two distinct mechanisms are illustrated in Fig. 1 where the planar region shows lower Y_e and denser material, while the polar regions have higher Y_e and less dense material.

We first consider the tidal ejecta. This kind of ejecta tends to be very neutron-rich, since it becomes unbound immediately during and following merger, and originates from matter near the surfaces of the stars. These tidal tails can be observed in the (x, y)-plane at 5 ms (top row) panels

of Fig. 1, where they are visible in the outer regions beyond 300 km. This ejected material also tends to be cooler, with a temperature of around 1 MeV. In contrast, in the (x, z)-plane, the Y_e reaches much higher values, approximately 0.3, that are not observed in the orbital plane. These higher values in the electron fraction are due to the shocked-heated material. In the polar regions right above the HMNS, no material is ejected tidally and neutrinos become free streaming very close to the merger product. As a result of weak interactions by means of which the free neutrons are converted into protons, the material becomes less neutron-rich. However, as the angle from the pole decreases, the material becomes more optically thick and more neutron-rich as the neutrino interactions are not as strong. This angular dependence is also seen in the temperature profiles as there are higher temperatures near the polar axis when compared with the orbital plane.

It is important to note here that although neutrinos are only treated simplistically [84] this broad-brush description is qualitatively similar to more sophisticated approaches such as those using an M1-scheme which lead to an increase in the amount of ejected material in the polar regions [23,26,115–117] and higher Y_e.

Turning to the effects of the EOS, there is a clear overall trend to be deduced from Fig. 1. The "softer" an EOS is, the hotter the matter tends to be. This is due to the fact that a softer EOS allows for a deeper gravitational well, which, in turn, allows for the material to become hotter. This dependence is clearest when comparing the softer SFHO and the stiffer LS220 EOSs (left and right columns),[2] where the temperature in the (x, y)-plane is much hotter for the SFHO than the LS220, as expected. As a result, because neutrino interactions depend on the temperature, the electron fraction is also higher the softer an EOS is. Again this is most clear when examining the fluid properties on the (x, y)-plane of the SFHO and LS220 simulations, where the data referring to the LS220 EOS is much more neutron-rich when compared with the SFHO.

V. MATTER-OUTFLOW PROPERTIES

This section is dedicated to a comprehensive discussion of the properties of the matter that is ejected dynamically in the merger and is unbound. In particular, we will concentrate on the total amount of ejected matter as well as on the distributions of this matter in terms of the electron fraction, of the specific entropy and of the velocity of the fluid elements.

A. Ejected-mass

An accurate measure of the total amount of ejected material from a binary merger is essential for the characterization of r-process elements and on the potential observable properties of kilonova (see Sec. VII). In Sec. III B, we defined the total ejected mass using outflow detectors which measure the flux of unbound material at a given radius. Hereafter, we consider the detector placed at a radius of 200 $M_\odot \approx 300$ km as the fiducial detector through which to measure the amount and properties of the ejected material. To compute the total mass ejected, the flux of the rest-mass density through the detector's spherical surface is computed and then integrated over the whole sphere. This gives the total mass-flux which can be integrated over time to provide a measurement of the total dynamically ejected material $M_{\rm ej}$. In this calculation, only the flux associated to unbound fluid elements contributes to the integral. Explicitly, for a detector at a given radial distance, the total ejected mass is given by

$$M_{\rm ej}(t) := \int_0^t \int_\Omega \rho_* W(\alpha v^r - \beta^r)\sqrt{\gamma}_\Omega \mathrm{d}\Omega \mathrm{d}t', \qquad (7)$$

where $\sqrt{\gamma}_\Omega$ is the surface element on the detector (i.e., the square root of the 2-metric induced on the detector by the spacetime 4-metric); the term $\rho_* W(\alpha v^r - \beta^r)$ is the flux of mass through the sphere, expressed in terms of the $3+1$ quantities: the lapse function α, the shift vector β^i, and the fluid 3-velocity v^i, the Lorentz factor $W := (1 - v^i v_i)^{-1/2}$ and the fraction of the rest-mass density that is unbound ρ_*, i.e., of fluid elements that do satisfy the geodesic criterion. The integral of the mass flux can then be integrated in time beginning at merger, i.e., $t = 0$ and ending at T_f, the time at the end of the simulation.

Figure 2 reports the amount of ejected material computed through Eq. (7) for the LS220 (blue), DD2 (green), and SFHO (red) EOSs and the different masses

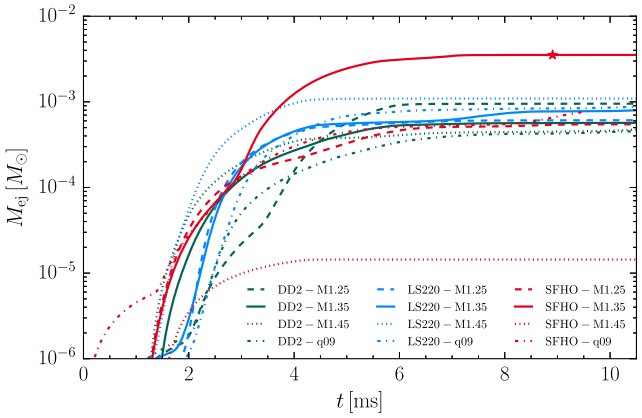

FIG. 2. Evolution of the dynamically ejected unbound mass $M_{\rm ej}$ as measured through a detector at radius 300 km when using the geodesic criterion and for the various binaries considered. The star denotes the time of black-hole formation for model `SFHO-M1.35`. Binaries `LS220-M1.45` and `SFHO-M1.35` collapse shortly after merger and are not visible in the plot.

[2]As discussed in Sec. II, the inclusion of light nuclei changes the composition, but not the temperature.

TABLE II. Summary of the mass-averaged quantities of Sec. V and kilonova observational quantities of Sec. VII computed from the simulations. The columns are, respectively: $M_{\rm ej}$ the dynamical mass ejecta measured at 300 km, $\langle Y_{\rm e}\rangle$ the mass-averaged electron fraction, $\langle s\rangle$ the mass-averaged entropy, $v_{\rm ej}$ the mass-averaged velocity of the ejecta, $\langle v_\infty\rangle$ the velocity of the ejecta at infinity using Eq. (9), $t_{H,\rm peak}$ the peak time in the H-band of the kilonova signal, $L_{\rm peak}$ the peak luminosity of the kilonova, $m_{X,\rm peak}$ the peak absolute magnitude in the $X = J, H, K$ bands respectively.

Model	$M_{\rm ej}$ $[10^{-3}\ M_\odot]$	$\langle Y_{\rm e}\rangle$ -	$\langle s\rangle$ $[k_{\rm B}]$	$\langle v_{\rm ej}\rangle$ $[10^{-1}$ c]	$\langle v_\infty\rangle$ $[10^{-1}$ c]	$t_{H,\rm peak}$ [days]	$L_{\rm peak}$ $[10^{40}$ erg/s]	$m_{J,\rm peak}$ [AB]	$m_{H,\rm peak}$ [AB]	$m_{K,\rm peak}$ [AB]
DD2-M1.25	0.96	0.13	13.9	2.3	1.7	0.50	2.24	−12.6	−12.5	−12.4
DD2-M1.35	0.58	0.14	16.5	2.4	1.8	0.50	2.44	−12.7	−12.7	−12.5
DD2-M1.45	0.50	0.17	19.2	2.7	2.1	0.50	2.89	−12.9	−12.9	−12.5
DD2-q09	0.46	0.14	18.5	2.3	1.7	0.53	2.34	−12.7	−12.6	−12.4
LS220-M1.25	0.61	0.08	10.3	2.2	1.6	0.53	2.24	−12.6	−12.6	−12.4
LS220-M1.35	0.82	0.10	12.7	2.2	1.5	0.51	2.00	−12.5	−12.4	−12.2
LS220-M1.45	1.09	0.11	10.5	2.6	2.1	0.48	2.62	−12.8	−12.7	−12.5
LS220-q09	0.90	0.09	11.9	2.2	1.5	0.50	1.94	−12.4	−12.3	−12.1
SFHO-M1.25	0.55	0.14	15.6	2.5	2.0	0.47	2.54	−12.8	−12.7	−12.5
SFHO-M1.35	3.53	0.16	12.7	2.7	2.2	0.53	3.36	−13.2	−13.2	−13.0
SFHO-M1.45	0.01	0.24	35.9	3.1	2.6	0.16	0.86	−11.1	−10.9	−10.5
SFHO-q09	0.76	0.16	18.8	2.4	1.8	0.60	2.92	−12.0	−13.0	−12.9

and mass ratios.[3] The results of Fig. 2 are also summarized in Table II, where $M_{\rm ej}$ refers to the mass ejected $t = 10$ ms after merger.

Overall, the qualitative behavior of all simulations is similar. There is a large ejection of material, due to tidal interactions and shock heating, that reach the detector approximately 1 ms after merger and continues for about 4–5 ms before the flux becomes zero. However, this apparent decrease in ejected material is simply due to the geodesic criterion not being satisfied by the outflowing material and not a physical decrease in outflow. In Appendix A, we discuss how this picture changes when considering the Bernoulli criterion, which allows for a longer period of ejected material.

Figure 2 shows that the amount of ejected material is in the range $0.5 - 1 \times 10^{-3}\ M_\odot$, with two exceptions. The first is the binary SFHO-M1.45, which collapses immediately to a black hole and results in very little material ejected (almost an order of magnitude less), as most is accreted onto the black hole. Conversely, the binary SFHO-M1.35 model ejects a significant amount of material when compared with the other models. Also this binary collapses to a black hole around 9 ms (see star symbol in Fig. 2) and since the SHFO EOS is a rather soft one, this HMNS is the most compact we have simulated. Under these conditions, it is natural that the larger compressions attained will lead to stronger shock heating and hence to a larger dynamical mass ejection.

[3]Unless specified otherwise, hereafter we will use the same color scheme to refer to the various EOSs: simulations with the LS220 EOS are shown blue, DD2 in green, and SFHO in red. Furthermore, the different masses are defined as follows, 1.25 $M_\odot$ is dashed, 1.35 $M_\odot$ is solid, 1.45 $M_\odot$ is dotted, and $q = 0.9$ is dash-dotted.

A measurement of the ejected mass that is alternative to that contained in Eq. (7) consists in evaluating a volume integral of the rest-mass density of the unbound material over the entire computational domain [23,54,55,118], i.e.,

$$M_{\rm ej}(t) = \int \rho_* W \sqrt{\gamma} \mathrm{d}^3 x. \tag{8}$$

As a cross-check we have employed this measurement for model LS220-M1.35 and found that $M_{\rm ej}(t)$ in this case is obviously not a monotonically increasing function of time, but reaches a maximum of $M_{\rm ej} = 0.80 \times 10^{-3}\ M_\odot$. This measurement differs only of 4% with that obtained via Eq. (7), demonstrating the robustness of our mass ejection and that the 300 km measurement radius is the most robust choice. In addition, the downside of the use of Eq. (8) is that because of the finite size of the domain, material that reaches the outer boundary is no longer include in the calculation and causes the total ejected mass to decrease. Due to this, we have evaluated Eq. (8) at ∼3 ms after merger where it reaches a maximum and thus introducing some level of arbitrariness in the evaluation of the integral. This specific arbitrariness does not arise with the flux-integral method (7), which is integrated over all time, but where a choice needs to be made for the extraction radius.

Finally, we note that our measured values of the ejected masses are systematically smaller than those reported in Ref. [23] for the same masses and EOS. This is likely due to the neutrino treatment employed here and to the fact that more-sophisticated M1-scheme with heating, such as that used in Refs. [23,26], can allow for material to be more energetic and hence to become more easily unbound [115]. On the other hand, our measurements agree with those of Ref. [55], where a similar leakage approach was employed;

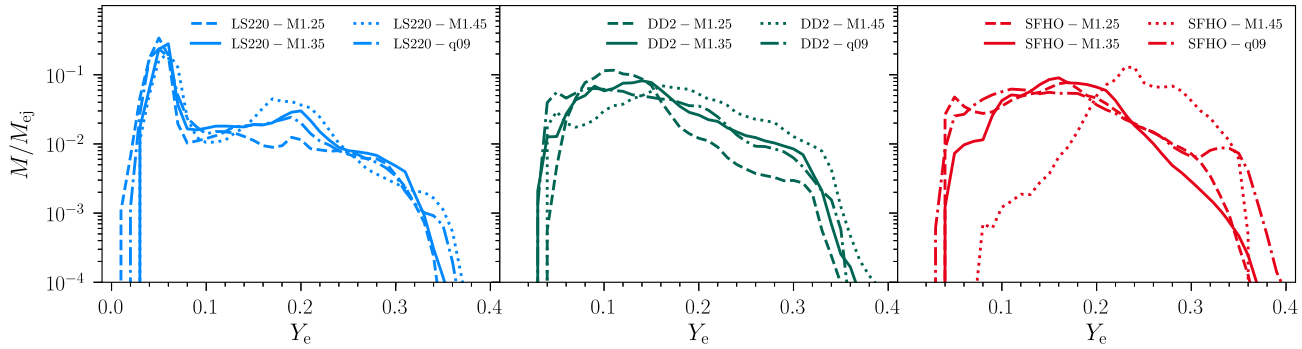

FIG. 3. Distributions of the ejected mass fraction as function of the electron fraction $Y_{\rm e}$, as measured by a detector at radius 300 km. The range of $Y_{\rm e}$ is divided into bins of width 0.01. The histograms are normalized over the total ejected mass $M_{\rm ej}$. The left panel refers to the DD2 EOS simulations, the middle one to the LS220 EOS and the right one to the SFHO EOS; different line types mark binaries with different masses and mass ratios.

at the same time, the preliminary use of an M0-scheme as that used in Ref. [24] is insufficient to explain this difference in the ejected mass. Finally, since the amount of the ejected material depends also on the specific properties of the computational infrastructure [e.g., the location of the extraction radius[4] in Eq. (7), or the size of the computational domain in Eq. (8)] only a direct comparison of the various neutrino-transport schemes within the same code can quantify the variance of the ejected matter on the neutrino treatment or the numerical specifications.

B. Electron-fraction distributions

The electron fraction is an important ingredient to determine the *r*-process nucleosynthesis yields since $Y_{\rm e}$ is effectively a measure of how many free neutrons are available. Typically, low-$Y_{\rm e}$ environments, i.e., with more free neutrons, favor a robust *r*-process and yield a higher fraction of heavier elements while in high-$Y_{\rm e}$ regimes, i.e., with less free neutrons, the production of very heavy elements tends to be suppressed. Differences in $Y_{\rm e}$ also correspond to potential differences in the properties of the resulting kilonova signal, due to the efficient production (or lack thereof) of high-opacity elements such as lanthanides. In particular, the so-called "blue" kilonovae (i.e., peaking at higher frequencies, in the optical band) are possible in environments with $Y_{\rm e} \gtrsim 0.25$ and "red" kilonovae (peaking in the infrared) in environments with $Y_{\rm e} \lesssim 0.25$ [27,32] (we will discuss the angular distributions of the thermodynamical quantities and their impact on the kilonova in Secs. VII and VII A).

Figure 3 shows histograms of the mass distribution of the ejected matter over the electron fraction for all 12 simulations, as computed from the data relative to our fiducial detector at radius 300 km; different panels refer to different EOSs, while the various lines refer to the different binaries we have evolved. In practice, each patch into which the detector sphere is subdivided, the local electron fraction value is recorded and the local amount of ejected mass is estimated. These values are then integrated over time up to T_f to produce the mass ejected along with the corresponding $Y_{\rm e}$; the resulting $Y_{\rm e}$ range is divided into bins of width 0.01 and the unbound mass of each patch at each time is assigned to a bin according to its corresponding value of $Y_{\rm e}$, thereby generating the histograms shown in Fig. 3.

Irrespective of the EOS and mass configuration of the runs, common qualitative features emerge. For all EOSs, the ejected mass is distributed in a range of $Y_{\rm e}$ varying from approximately 0.04 up to 0.4, peaking at $Y_{\rm e} \lesssim 0.2$. The only exception is the `SFHO-M1.45` model, which ejects little material due to black hole formation and whose distribution peaks at higher values of $Y_{\rm e}$. This spread of the electron fraction over a wide range is due to the inclusion of a neutrino treatment, which causes the number of electrons to change due to weak interactions. Failure to take such interaction into account would result in a very different distribution, sharply peaked at very low values of $Y_{\rm e}$, i.e., pure neutron matter (see, e.g., Ref. [24]).

More in detail, the LS220 runs (left panel) exhibit very similar distributions for all mass configurations, peaking at approximately $Y_{\rm e} = 0.05$ with a secondary peak at $Y_{\rm e} \approx 0.2$ before sharply dropping off at electron fraction values of $Y_{\rm e} \gtrsim 0.3$. The distributions of the DD2 (middle panel) also all exhibit a similar behaviour, with a sharp increasing at $Y_{\rm e} \sim 0.05$ before broadening out with a sharp drop around $Y_{\rm e} \sim 0.3$. Finally, the distributions of the SFHO runs (right panel) exhibit a somewhat different behavior, although spanning a similarly broad range in $Y_{\rm e}$. The main differences in this case are the tail of the distribution at higher values of the electron fraction. In all cases, most of the ejected matter is found at low values of the electron fraction, i.e., it is very neutron-rich, which suggests a robust *r*-process in all of the cases considered here.

[4]In our calculations we have found that the difference between the sphere at 300 km and a sphere at 740 km is about 30% irrespective of EOS. Although the sphere further away has a slightly higher ejected mass, the properties of the fluid are very close to atmosphere at these radii and should be avoided.

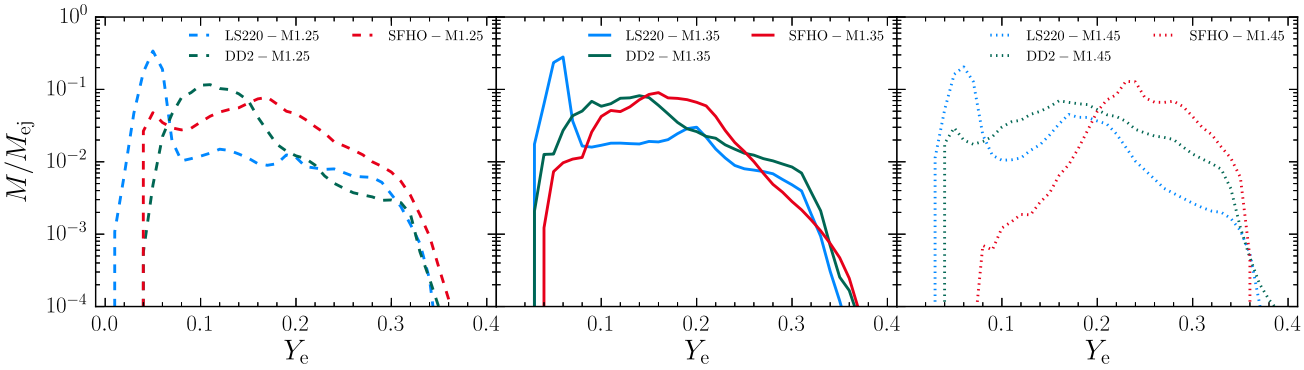

FIG. 4. Distributions of the ejected mass fraction as function of the electron fraction $Y_{\rm e}$, as measured by a detector at radius 300 km. This is the same as Fig. 3, except that the curves are here grouped by mass configuration rather than EOS so as to highlight the dependence on the latter. For clarity, unequal-mass binaries are not shown.

This conclusion is also supported by Table II, where the average values $\langle Y_{\rm e}\rangle$ of the electron fraction are reported for all 12 runs. The averages are computed over the mass/electron fraction histograms of Fig. 3. As can be seen in all simulations, the average value of the electron fraction in the ejecta is approximately 0.15 or lower, indicating on average a very neutron-rich environment. The only exception is model `SFHO-M1.45` where $\langle Y_{\rm e}\rangle = 0.24$.

In Fig. 4, to help the comparison of the results across different EOSs the distributions are arranged according to the total mass of the BNS (the unequal-mass cases are excluded) instead of EOS in Fig. 3. In all panels, there is a noticeable trend in the distributions of $Y_{\rm e}$, which is most evident in the 1.25 $M_\odot$-case (left panel), where $\langle Y_{\rm e}\rangle = 0.08$, 0.13, and 0.14 for LS220, DD2, and SFHO EOSs, respectively. This increase in $Y_{\rm e}$ is expected when considering that neutrino interactions depend strongly on the temperature. The average entropy (see Sec. V C) of these simulations is 10.3, 13.9, and $15.6k_{\rm B}$ respectively. Entropy is related to temperature and the higher the entropy, the higher the average temperature, cf., Fig. 3, and hence more free neutrons are converted into neutrinos through positron capture, increasing $Y_{\rm e}$.

This effect is also related to the compactness of the object, albeit this relation should be treated carefully. SFHO is the softest EOS, which leads to the most compact objects. This results in higher temperatures during the merger, which causes an increase in the neutrino reactions, which decreases the number of neutrons and as expected has the highest average $Y_{\rm e}$. In contrast, from Table I one would expect that because LS220 is more compact than DD2, LS220 should have a higher average $Y_{\rm e}$ and entropy when the opposite is this the case. This difference is due to compactness being a property calculated for cold beta-equilibrium where the effects of composition are minimal. As discussed in Sec. II, the LS220 does not include light nuclei which can change the composition and the neutrino interactions so this seemingly non-monotonic relation between compactness and average $Y_{\rm e}$ arises from different constructions of the EOS. When comparing DD2 and SFHO and excluding LS220, there is a clear monotonic relationship between $\mathcal{C}$ and $Y_{\rm e}$.

When comparing our results with that of simulations with similar initial data, there is a disagreement with computed values of the electron fraction. For example, for the `DD2-M1.35` model with our measured value of $\langle Y_{\rm e}\rangle = 0.14$, the authors of Ref. [23] report $\langle Y_{\rm e}\rangle = 0.29$ with an M1-scheme independent of resolution and $\langle Y_{\rm e}\rangle = 0.26$ with a leakage scheme with a resolution of 200 m. However, a similar distribution in $Y_{\rm e}$ is observed in Refs. [55,119], which use a similar leakage scheme to the one used here.

C. Specific-entropy distributions

The next thermodynamic quantity we consider is the distribution of the ejected material over the entropy per baryon s. The specific entropy is important in r-process nucleosynthesis as it impacts the neutron-to-seed ratio, with high initial neutron-to-seed ratios favoring the production of heavy nuclei during the r-process nucleosynthesis even at relatively high electron fractions. In particular, in radiative environments such as those accompanying the ejected matter, the specific entropy will scale with the temperature as $s \propto T^3$, so that the shock-heated (and hotter) part of the dynamical ejecta will exhibit higher entropies. In turn, because the seed nuclei will be photodissociated at high temperatures, a higher specific entropy will increase the neutron-to-seed ratio and thus r-process nucleosynthesis. In contrast, the cold, tidal dynamic ejecta, and which dominates the unbound matter in Newtonian simulations, (see, e.g., Refs. [47,110,120]) usually exhibit low entropy, but extremely neutron-rich material [72]. The distributions of the specific entropy computed with the same procedure as the electron fraction distribution in the previous section, is shown in Fig. 5, while the average values $\langle s\rangle$ are reported in Table II.

Again, we observe many EOS-independent qualitative features. First, for all EOSs, the mass distribution peaks at

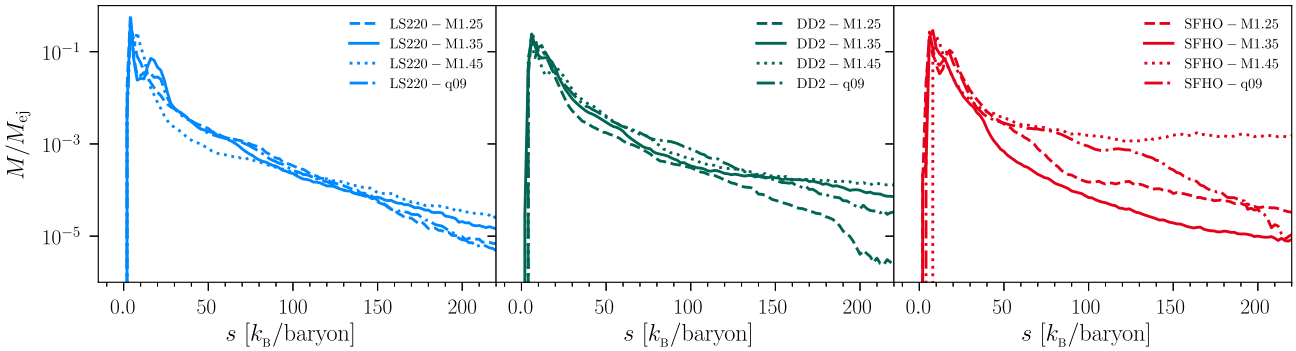

FIG. 5. The same as in Fig. 3 but for the specific entropy s. The range of s is divided into bins of width $2k_{\rm B}$ and the histograms are normalized over the total ejected mass.

$s \approx 2k_{\rm B}$, while a fast decay is visible towards higher entropies. In the case of the binaries with the DD2 EOS (middle panel), the qualitative behaviour of different mass configurations is similar up to approximately $s \simeq 100k_{\rm B}$. At larger entropies, the `DD2-M1.25` binary has a more rapid drop-off and there is very little material that reaches higher entropies. In comparison, the remaining models exhibit similar behavior with a flattening of the curve at higher entropies. The average entropy value is in all four cases $\langle s \rangle \approx 15k_{\rm B}$. Second, all of binaries with the LS220 EOS (left panel), show a very similar qualitative behavior among themselves and strong analogies with the DD2 binaries. In particular, the distributions show a rapid increase in entropy at around $2k_{\rm B}$ (for the 1.45 $M_\odot$ binary this peak is at around $8k_{\rm B}$ and is 4 times smaller), with an additional second peak at $20k_{\rm B}$ for the 1.35 $M_\odot$ case that is not present in the other masses. For all masses, there is a rapid decrease in specific entropy, with average entropies that are slightly lower than the DD2 and SFHO binaries and with a smaller spread between the values, being approximately $s \sim 11k_{\rm B}$.

Finally, the simulations with binaries having the SFHO EOS (right panel) show a similar qualitative behaviour with the other runs, at least at low entropies. The distributions peak at about $5k_{\rm B}$ and a rapid drop follows, although different binaries show different fall-offs at around $50k_{\rm B}$. In the `SFHO-M1.25` case, the distribution begins to decrease less rapidly at higher entropies while the `SFHO-M1.35` model shows the fastest decrease. This is in contrast to the DD2 and LS220 simulations (where the specific entropies correlate with the initial masses of the stars) and is reflected in the average values of the specific entropy, with the `SFHO-M1.25` model having $\langle s \rangle = 15.6k_{\rm B}$, while `SFHO-M1.35` a smaller value of $\langle s \rangle = 12.7k_{\rm B}$. Lastly, the average specific entropy of the `SFHO-M1.35` binary is almost twice as large, likely due to the fact that the small amount of ejected matter has been efficiently heated on account of its rarefaction. While somewhat puzzling, this nonmonotonic behavior of the specific entropy with the SFHO binaries is likely due to the comparative softness of this EOS, which enhances the nonlinearity associated with shock-heating effects.

Indeed, as with the electron-fraction distributions, the average entropy tends to increases with the softness of the EOS,[5] being the highest for the softest EOS, i.e., SFHO. For example, concentrating on the 1.25 $M_\odot$ binaries, $\langle s \rangle = 10.3, 13.9, 15.6k_{\rm B}$, for the LS220, DD2, SFHO EOSs, respectively. This dependence is not particularly surprising as softer EOSs produce a higher temperature and the temperature is directly related to the specific entropy. This relation holds for almost all cases, even when including the low-mass ejecta of `SFHO-M1.45`; the only exception is offered by the `SFHO-M1.35` binary, where this discrepancy is likely due to there being at least 5 times as much ejecta as the other binaries.

D. Ejection-velocity distributions

Figure 6 reports the velocity distributions of the ejecta computed in full analogy with the electron-fraction or specific-entropy distributions presented in the previous two sections. Note that unlike, e.g., Ref. [24], we here distinguish between the velocity of the ejected material $v_{\rm ej}$ as measured in the simulation and that of the ejecta at spatial infinity $v_{\rm inf}$. In particular, we compute $v_{\rm ej}$ directly from the Lorentz factor W, i.e., $v_{\rm ej} = [(W^2-1)/W^2]^{1/2}$, where we assumed that the detectors are sufficiently far away from the merger product so that the Minkowski metric holds. As discussed in Ref. [71], this is a rather good approximation since it was shown there that the ejected matter moves essentially radially and there is only a subdominant velocity component in the angular directions, hence $v^2 \approx v_r^2$, which enables us to compute $v_{\rm ej} \simeq v^r$ from W. An obvious consequence of distinguishing between $v_{\rm ej}$ and $v_{\rm inf}$ is that our values of the ejecta velocities are systematically higher than in Ref. [24].

[5]Taking into consideration the caveats at the end of Sec. V B.

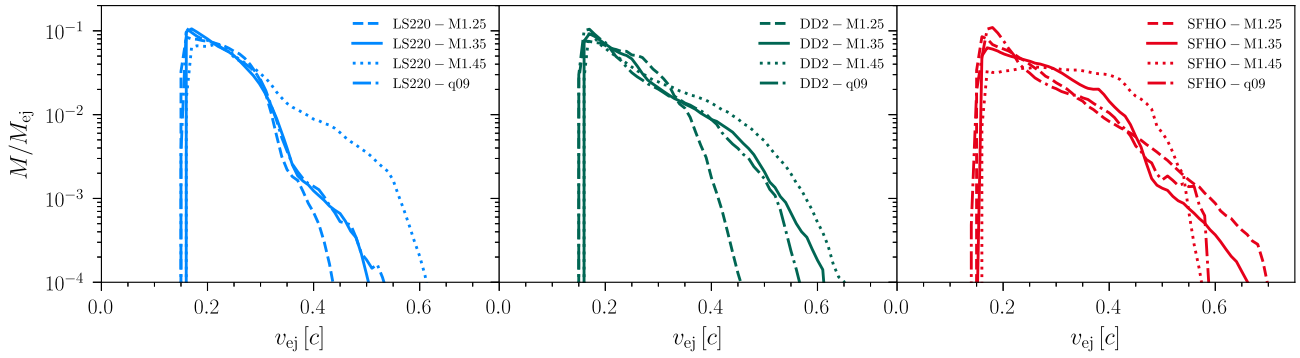

FIG. 6. The same as in Fig. 3 but for the ejecta velocity $v_{\rm ej}$. The range of $v_{\rm ej}$ is divided into bins of width 0.05 and the histograms are normalized over the total ejected mass.

Again, Fig. 6 reveals that every simulation exhibits similar qualitative behavior. The ejecta velocity is never lower than $0.15c$; the bulk of the matter has velocities of $v_{\rm ej} \approx 0.25c$, and at higher velocities of $v_{\rm ej} \gtrsim 0.6c$ the mass distribution quickly drops to zero. Table II reports the average velocity $\langle v_{\rm ej} \rangle$ for all the runs. A trend clearly emerges from our data, with the higher-mass configurations systematically producing higher-ejecta velocities. More precisely, the ejecta velocity appears to be tightly correlated with the compactness of the neutron stars involved in the merger (cf., Table I). Also in this case, this trend is not particularly surprising since higher-mass configurations result in more compact starts, which in turn experience stronger torques and more efficient shock heating.

In Table II, the column denoted by $\langle v_\infty \rangle$ shows estimates of the ejecta velocity at infinity, which is achieved in the homologous expansion phase. This velocity is used in our approximate model of kilonova emission (see Sec. VII) and is computed assuming a ballistic radial motion from $r = 300$ km to infinity in the spherically symmetric gravitational field of an object with the same ADM mass of the BNS system under consideration, i.e.,

$$\sqrt{1-\frac{2M_{\rm ADM}}{r}}\frac{1}{\sqrt{1-\langle v_{\rm ej}\rangle^2}} = \frac{1}{\sqrt{1-\langle v_\infty\rangle^2}}. \qquad (9)$$

In the Newtonian limit, $M_{\rm ADM} = M$ and expression (9) simply reduces to the familiar energy conservation equation: $\frac{1}{2}\langle v_{\rm ej}\rangle^2 - GM/R = \frac{1}{2}\langle v_\infty\rangle^2$.

VI. *r*-PROCESS NUCLEOSYNTHESIS

This section is dedicated to the *r*-process nucleosynthesis of the matter ejected dynamically. In particular, we will concentrate on the optimal selection of the tracers, on how nucleosynthesis varies with the specific entropy of the ejected matter and on those behaviors that are essentially independent of the EOS.

A. Tracer-input comparison

In Sec. III B we introduced a method to associate a mass to the otherwise massless tracers. Here, we introduce two additional tracer-selection criteria (together with the unboundness criterion already discussed and which is always enforced) and the corresponding procedures to associate a mass to the tracers; we then compare the impact that this different selection strategies have on the final nucleosynthesis yields.

We recall that the first criterion, introduced in Sec. III B, consists in considering from a given simulation all tracers that are unbound, associate to each of them a mass by locally integrating a mass flux through a sphere of given radius as in Ref. [71] (in our case, the sphere is the fiducial outflow detector at radius 200 $M_\odot$), then sum the nucleosynthesis yields from all tracers using the corresponding mass as weight to recover the final abundance pattern. Since the total number of unbound tracers in one of our simulations can reach several thousands (40,000 being a typical value), this approach involves the post-processing and book-keeping of many tracer trajectories, thus becoming computationally rather costly. For this reason, we develop the alternative selection criteria described below.

The second tracer-selection criterion consists instead in considering the distributions of the ejected mass as a function of the electron fraction presented in Sec. V B and in drawing one representative, unbound tracer from each bin. Given the bin width of $\Delta Y_{\rm e} = 0.01$, this results in about 40 tracers for every simulation, a reduction of a factor of a thousand with respect to the first criterion. In this approach a mass is then associated to each tracer by assigning to it the mass of the bin it was drawn from. We refer to this procedure as to the "1D" criterion, since the tracers are drawn from a 1D distribution.

We finally consider a third selection criterion, essentially an improved version of the 1D criterion. It consists in considering the ejected mass histogram over both the electron fraction and the specific entropy; we then draw one representative, unbound tracer from each bin, and associate to it the mass of the bin it was drawn from.

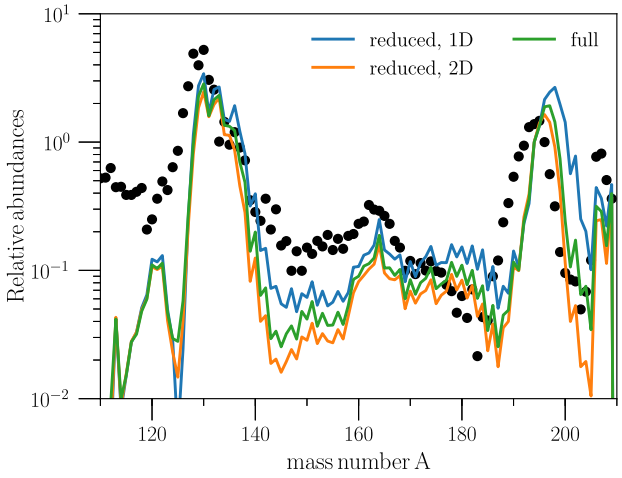

FIG. 7. Comparison of the relative abundances Y_i of the r-process as function of the mass number A for the three tracer selection criteria. In blue, the abundances produced by the "1D" criterion; in orange the ones produced by the "2D" criterion; in green the abundances obtained considering all unbound tracers. The black filled circles indicate the solar abundances.

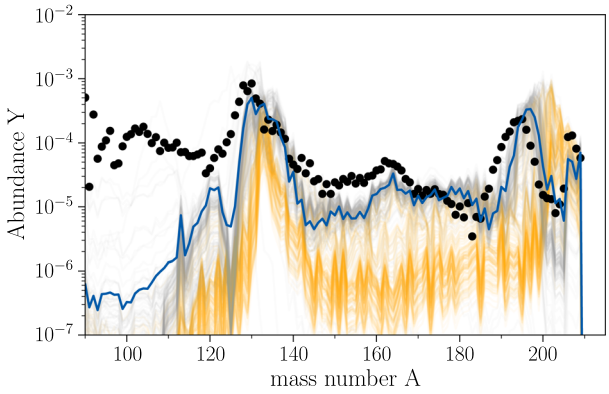

FIG. 8. Final r-process abundances for all unbound tracers of the LS220-M.1.35 binary. Gray lines are the yields for individual tracers with low entropies $s < 70k_B$, and orange lines mark single tracers with high entropies $s \geq 70k_B$. The mass-integrated nucleosynthesis yields are shown with a blue line, and the black filled circles show the solar abundances.

We refer to this procedure as to the "2D" criterion, since the tracers are drawn from a 2D distribution. For each simulation, this results in a total of roughly 1,000 tracers to be considered.

We show in Fig. 7 the results from the nucleosynthesis calculations for the three selection criteria. Following [71], we restrict the comparison to one fiducial case, the binary LS220-M1.35, and compare our final abundance pattern with the solar one (filled circles), showing the relative difference to it in the bottom panel. As can be seen, the original approach of considering all unbound tracers reproduces quite well the solar abundances over the whole range of mass numbers considered, as does the 2D criterion. The 1D criterion instead shows significant deviations, especially around the third peak (i.e., $A \simeq 195$) and around the rare-earth peak (i.e., $A \simeq 165$). *A posteriori*, this is due to the fact that the 1D criterion is systematically biased toward low-entropy tracers, which has a significant impact over the final abundances, as we discuss in the next section.

The 2D criterion is computationally much less expensive than considering all unbound tracers, it allows for a simple and unambiguous definition of the tracer mass, and yet it leads to an almost unbiased abundance calculation. In the following, we adopt it as our preferred tracer-selection criterion and compute all results with it, unless otherwise stated.

B. Heavy-element nucleosynthesis

Figure 8 illustrates the nucleosynthesis results for all ∼40,000 unbound tracers of the representative simulation of the LS220-M.1.35 binary. In particular, we plot individual tracers with $s < 70k_B$ in gray or $s \geq 70k_B$ in orange, respectively, alongside the mass-integrated abundances (blue line). As a consequence of the relatively low electron fractions for most of the ejecta (i.e., with $Y_e \approx 0.1$; see Fig. 3 and Table II), for each tracer, the strong r-process component (from the second to the third r-process peak) is well reproduced. At the same time, we find that the entropy distribution of the ejecta gives rise to specific features in the abundances pattern. More specifically, the low-entropy component (i.e., $s < 70k_B$) leads to the pattern that is observed in the neutron-rich ejecta of Newtonian simulations. On the contrary, the high-entropy (i.e., $s \geq 70k_B$) part of the ejecta, which carries only about 6% of the total ejected mass, has a nucleosynthesis pattern with a shifted second and third peaks. Additionally, it shows diminished abundances in the rare-earth region, and effectively fills the gap between the third r-process peak and elements in the lead region. We note that the abundance pattern of these tracers is very similar to the "fast" ejecta found by the authors of Ref. [121]. While we do not find them to expand faster in the beginning, their unusual abundance distribution can be traced back to an extremely high initial neutron-to-seed ratio $Y_n/Y_{seed} \gtrsim 1,000$ and comparably low initial densities $\rho \lesssim 10^9$ g/cm^3. Due to the enormous amount of neutrons at low densities, the seed nuclei require substantially more time to incorporate the neutrons, delaying the freeze-out time (i.e., the time when $Y_n/Y_{seed} = 1$). In fact, the time window for the r-process to occur in this minority of ejected material is $\gtrsim$100 s instead of $\lesssim$1 s. Moreover, the r-process runs along a path much closer to the valley of stability for these tracers, such that the magic neutron numbers are reached at higher mass numbers, and the abundances settle down for a pattern in between s-process and r-process.

Figure 9, on the other hand, reports the final heavy-elements relative abundances for all of the 12 BNS models outlined in Table I and shows them as a function of the

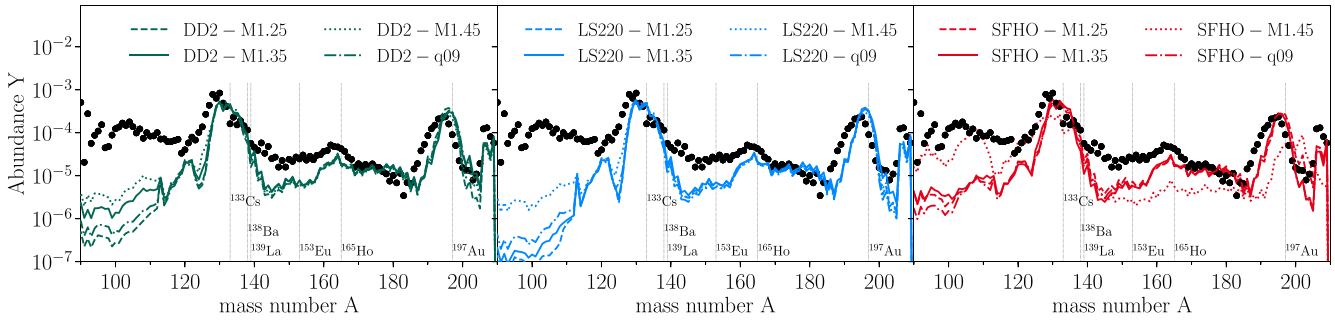

FIG. 9. Final relative heavy-elements abundances for all the 12 BNS models as a function of mass number A. The abundances are normalized so that the total mass fraction is unity, while the different panels and lines refer to the various EOSs, masses and mass ratios, respectively (see legends). The black filled circles report instead the observed solar abundances, while the vertical lines mark a few representative r-process elements: ^{133}Cs, ^{138}Ba, ^{139}La, ^{153}Eu, ^{165}Ho, ^{197}Au.

mass number A. As in previous figures, the different panels refer to the different EOSs considered and the various binaries are represented with lines of different types. Furthermore, the results are normalized to have a total mass fraction of 1 and shown with filled circles are the scaled solar system r-process abundances. Clearly, in all cases, a successful r-process is obtained, leading to the production of the r-process pattern from the second (i.e., $A \sim 130$) to the third (i.e., $A \sim 195$) peak.

However, there are different admixtures due to the different electron-fraction distributions of the ejected material as detailed in Sec. V B. For the equal-mass binaries, in particular, we observe a tendency of slightly enhanced abundances below the second r-process peak with increasing mass of the neutron stars. This is because more massive BNS systems have a higher electron fraction on average. Furthermore, the contributions from tracers with high initial neutron-to-seed ratios enhance both the second r-process peak and the region with $A \approx 200$ in all cases. The most extreme example is the `SFHO-M1.45` binary, which immediately collapses to a black hole after merger, ejects very little mass and with a comparatively high electron fraction. As a result, the part of ejected material with low specific entropy leads to nuclei that mainly have mass numbers with $A \lesssim 130$, while the material with high specific entropy—and thus high neutron-to-seed ratios—dominates the final abundances beyond the third r-process peak, leading to an enhanced abundance for $A \gtrsim 200$. The distinctive features observed in the final abundances in the case of the `SFHO-M1.45` binary opens therefore the prospect of using the chemical yields either as a confirmation of the prompt production of a black hole after the merger, or as an indication of this process in the case in which the postmerger gravitational-wave signal is not available.

All things considered, the most striking result shown in Fig. 9 is the very good and *"robust"* agreement of the various abundance patterns, where by "robust" we mean a behavior that is only very weakly dependent on the EOS or the initial neutron-star masses, at least for the sample considered here. For example, when considering the second peak at $A \sim 130$, all four different types of initial data predict a similar abundance of ^{133}Cs. Although the lanthanides show a slight disagreement with the solar abundances around the mass number $A \sim 145$ (which may be explained by other forms of ejecta, for example from accretion disks [122]), from ^{153}Eu up ^{197}Au in the third r-process peak, there is no disagreement in the final abundances for different initial data and EOSs.

While this agreement might be partly aided by our simplified neutrino treatment, this result not only confirms the robustness of the r-process yields from BNS mergers already noted in the literature, but it also shows how the uncertainties associated in modeling the microphysics and initial data of BNS mergers have a very limited impact on the nucleosynthesis produced from the merger. As we will discuss in Sec. VII, although the final abundance curve is essentially independent of the initial data and EOS, the kilonova light curves produced from the decaying elements depend strongly on these parameters and thus allow for a way to distinguish between the different scenarios.

In fact, the spread in our r-process patterns is much less than the one associated to uncertainties in the nuclear-physics modeling of nuclei involved in the r-process, e.g., the choice of the fission fragment distribution [123] or the nuclear-mass model (see, e.g., Refs. [124,125]) where variations can change the abundance of a given element by an order of magnitude.

VII. EJECTA MORPHOLOGY AND KILONOVA LIGHT CURVES

A. Angular distributions of ejected matter

The use of outflow detectors allows us to study, in addition to the properties of the ejected material, the angular distribution of the ejected material on the detector surface and hence virtually at spatial infinity. Besides having an interest in their own right, anisotropies in the distribution of the ejected matter could have important consequences on the kilonova signal of a given binary

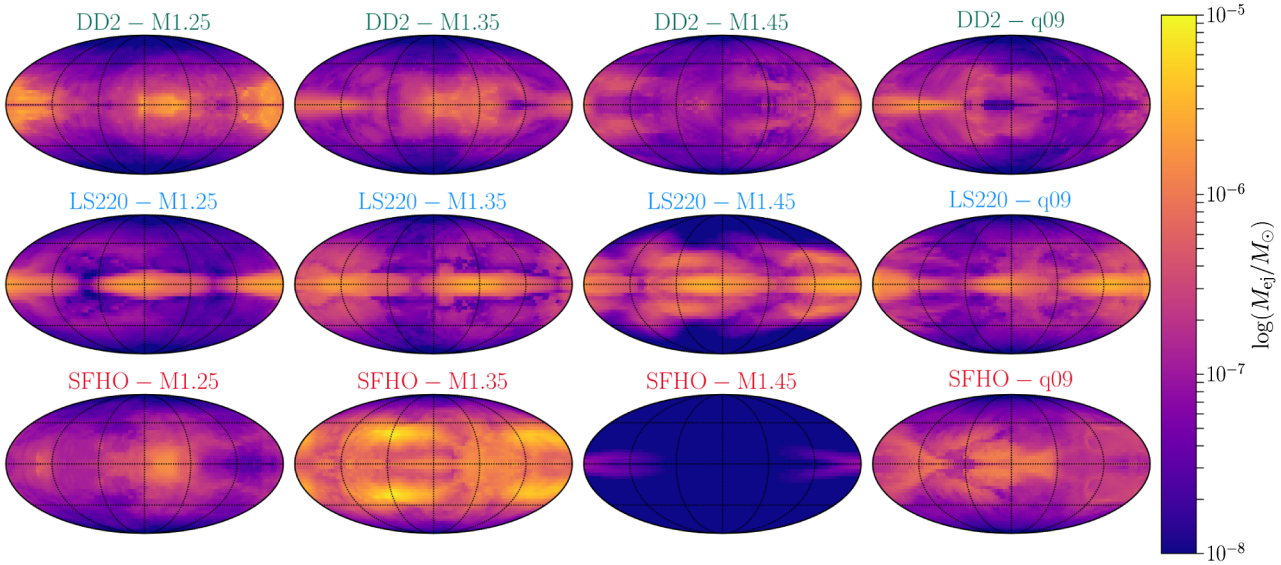

FIG. 10. Angular distribution of the ejected mass at the final time for the various binaries, with the different rows referring to the different EOSs considered.

configuration, and impact its detectability. To the best of our knowledge, this is the first time that an analysis of this type has been carried out.

In practice, we consider the angular distribution of ejected mass as defined by Eq. (7), where in this case however the integration over the angular directions does not span the whole 2-sphere, but only a single patch of the outflow detector. We also study the mass-averaged distribution of the electron fraction, the specific entropy and the ejecta velocity. Similarly to Eq. (7), these are defined as

$$\langle \chi \rangle := \int_0^{T_f} \int_{\Delta\Omega} \chi \rho_* W(\alpha v^r - \beta^r) S d\Omega dt / \int_0^{T_f} \int_{\Delta\Omega} \rho_* W(\alpha v^r - \beta^r) S d\Omega dt, \quad (10)$$

where χ is any one of Y_e, s or v_{ej}, and the same consideration as above applies to the integration over the angles. In this section we only focus on the results obtained for the angular distribution of the ejected mass and the electron fraction. The corresponding analysis in the case of the specific entropy and of the ejecta velocity is reported in Appendix B.

In Fig. 10, we report Mollweide projections of the outflow detector relative to the time-integrated rest mass for all models. Several observations are in order: First, the binary `SFHO-M1.45`, which immediately collapses to a black hole after the merger, is immediately identifiable as there is close to no ejected matter in this case. Second, it is clear that, in each binary, most of the mass is ejected on the orbital plane, which is consistent with expectations that the material ejected here is mostly of dynamical origin and is powered by the torques in the system at merger (other types of ejecta, such as neutrino/magnetically driven winds or ejecta from viscous heating could display a more isotropic structure). Third, while concentrated at low latitudes, the ejected mass is not uniformly distributed but shows considerable anisotropies; this is simply due to the disruption flows produced by the tidal torques and this concentrates the emission of matter into rather small regions on the detector surface. The only binary that appears to evade this trend is `SFHO-M1.35`, which has ejected also at latitudes as high as ∼45° and seems to peak around ∼30°.

Similarly, the distribution of the electron fraction Y_e is shown in Fig. 11. It can immediately be appreciated how the electron fraction tends to anticorrelate with the amount of ejected mass: regions in which the ejected mass fraction is higher (such as the orbital plane) tend to have very low Y_e and vice versa. This consistent with the results of Sec. V B, where most of the ejected mass was shown to be very neutron-rich. On the other hand it can be seen that in other regions, such as the poles, the material is very neutron-poor, but has correspondingly low values of ejected mass. The evidence provided in Fig. 11 that matter ejected around the poles is less neutron-rich (i.e., with $Y_e \gtrsim 0.25$) suggests the possibility that material there might undergo a less robust r-process, leading to a suppressed production of lanthanides and thus to a lower opacity. This bimodal anisotropy in the distribution of the electron fraction could then lead to either a "blue" kilonova, i.e., to a kilonova signal with a comparatively strong optical component, if the line of sight is mostly along the polar regions, or to a "red" kilonova, i.e., to a kilonova signal peaking in the infrared, if the line of sight is mostly along the equatorial regions [28,32].

We have checked the plausibility of such a scenario by explicitly computing the angular distribution of the

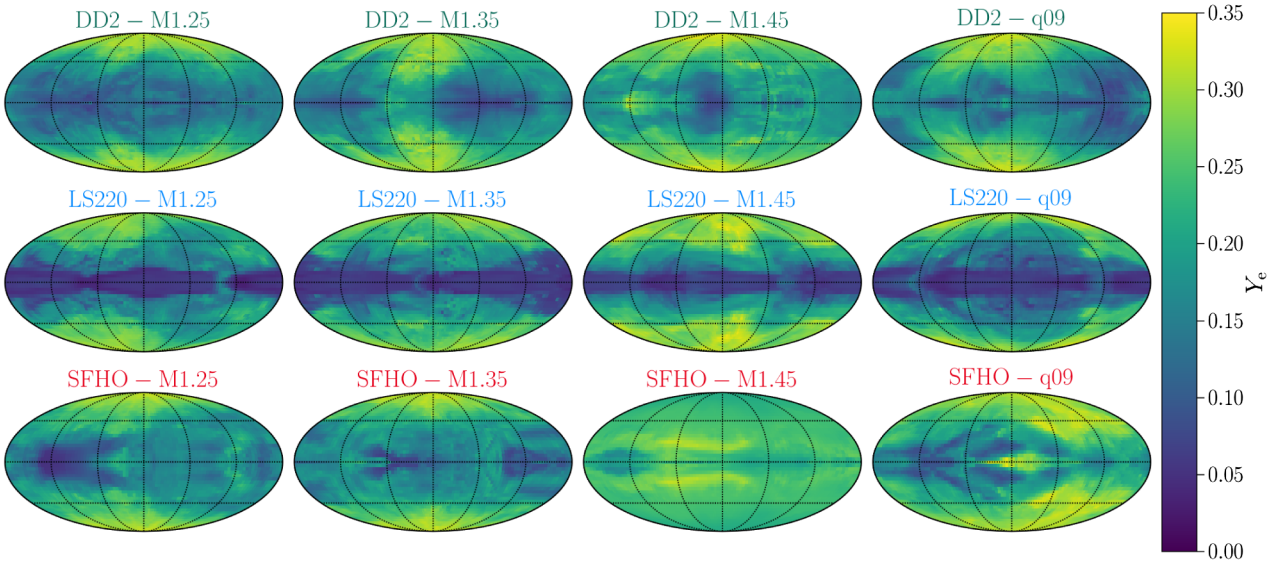

FIG. 11. The same as in Fig. 10 but for the electron fraction.

lanthanides mass fraction in the representative `LS220-M1.35` model. This has been obtained by computing the lanthanides mass fraction of every unbound tracer in the simulation and by plotting their location on the 2-sphere, as shown in Fig. 12, where the lanthanides mass fraction values have been averaged over patches of angular size $10° \times 10°$. As can be seen from the figure, even near the poles, the lanthanides mass fraction is rather high, i.e., $X_{\rm La} \approx 10^{-2}$. This is far larger than the generally accepted limit on this value that leads to a sufficient suppression of the medium opacity for a blue kilonova to be observed, i.e., $X_{\rm La} \sim 10^{-5}$. Very similar values have been obtained in all other BNS models.

Our results, therefore, seem to indicate that a blue-kilonova scenario is probably unlikely to originated from the dynamical ejecta in view of GW170817 [126]. As a word of caution, however, we note despite the three orders of magnitude difference between the expected value and the one computed here, our conclusions may be biased by an oversimplified neutrino treatment. A proper neutrino-transfer treatment of the propagation of neutrinos in the ejected matter could in fact modify, at least in part, our results. Indeed, a more sophisticated neutrino treatment, such as the one employed in Ref. [117], can result in a higher values of the electron fraction around the polar regions. All things considered, our results suggest that while a blue kilonova component cannot be ruled out conclusively, it also seems to require an electron-fraction distribution that is considerably different from the one computed here.

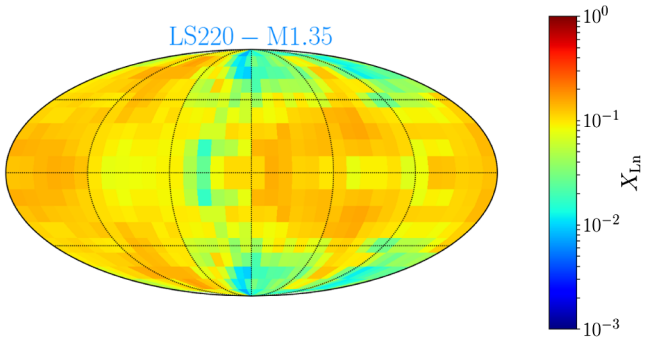

FIG. 12. Angular distribution of the mass fraction of lanthanides in the representative case of the binary `LS220-M1.35`; the data refers to the final simulation time.

B. Kilonova observability

We assess the observability of the infrared transients associated to the decay of *r*-process elements using the simple gray-opacity model of kilonovae developed in Ref. [19]. The small ejected masses resulting from our simulations preclude the use of more sophisticated radiative-transfer treatments (which we leave for a future work) when these ejecta could be a significant source of opacity (the "lanthanides curtain") for potential secondary outflows, such as magnetically [64] and viscously driven wind from an accretion disk, or neutrino-driven wind from the hypermassive neutron star [20].

In the model of Ref. [19], the background dynamical ejecta are approximated by a homologously expanding spherically symmetric solution $\rho(r,t) = \rho_0(t_0/t)^3 \times (1 - v^2/v_{\rm max}^2)^3$ (also described in detail in Ref. [31]), and $v_{\rm max} = 2\langle v_\infty \rangle$ from Table II. The luminosity output is computed by integrating the nuclear heating rate from the nuclear network over the layer of matter from which photons can diffuse out; a similar model was used also in Refs. [20,30,58]. We employ an effective gray opacity $\kappa = 10\ {\rm cm^2\ g^{-1}}$, which was recently demonstrated to reproduce reasonably well the infrared luminosity of

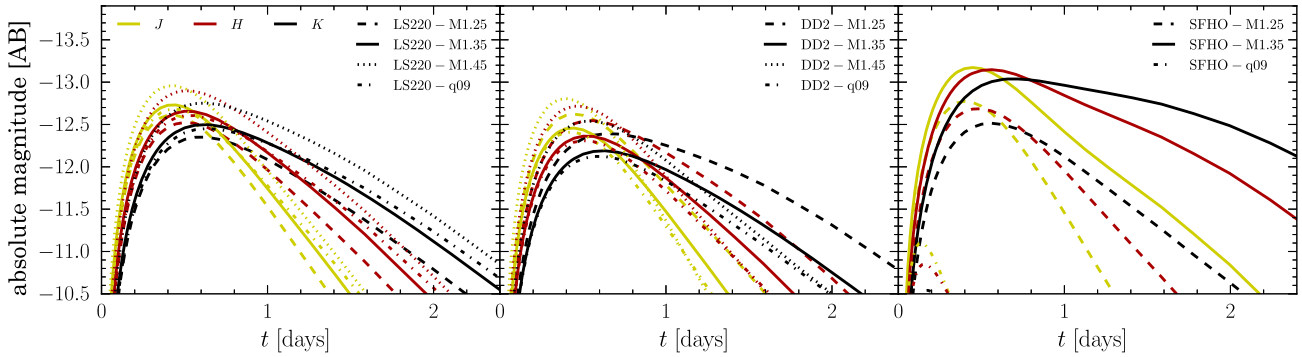

FIG. 13. Synthetic light curves in the infrared 2MASS J, H and K-bands for all of the binaries considered.

lanthanide- and actinide-contaminated ejecta [31]. We note that the same study has shown how the flux in the optical bands is strongly suppressed when detailed opacities of lanthanides are used; For this reason, we consider here only the infrared magnitudes J, H and K-bands in the Two Micron All Sky Survey (2MASS) [127].

The nuclear heating which powers the kilonova for each model is calculated with the nuclear network code WinNet [43,72], cf., Sec. III D, using the average electron fraction $\langle Y_e \rangle$, specific entropy $\langle s \rangle$ and expansion velocity $\langle v_\infty \rangle$ as given in Table II. We compute the nucleosynthesis yields with reaction rates based on the finite-range droplet model (FRDM) [128] only. This is motivated by the fact that nuclear mass models show little discrepancy in the heating rates at epochs around $t \simeq 1$ day [30], where the peak magnitudes for our models are expected.

The resulting peak bolometric luminosities, peak magnitudes in the infrared bands, and the peak epochs in the H-band are presented in Table II, while the light curves in the three infrared bands (different line colors) are shown in Fig. 13, with different line types referring to the different binaries.

Clearly, all of our models show a very similar behavior, peaking around half a day in the H-band and rapidly decreasing in luminosity after one day, reaching a maximum magnitude of -13. We note that these luminosities are smaller than those normally expected (see, e.g., [28] for a recent review), which peak around magnitude of ~ -15; this difference, however, is not surprising and is mostly due to the amounts of ejected mass, which is normally assumed to be $\sim 10^{-2}\ M_\odot$ and hence at least one order of magnitude larger than what measured here. With 3-minute J-band exposure on the VISTA telescope [129], these magnitudes result in a detection horizon of ~ 100 Mpc, which, in combination with a very short time around the peak, makes these light curves extremely difficult to detect in a follow-up survey. As observed in the follow-ups to GW170817, light curves were observed that originate from a kilonova [1,126,130] which suggests that a significant amount of material, on the order of $10^{-2}\ M_\odot$, became unbound. As this amount of ejecta is above the amount we have seen in dynamical merger simulations, this suggests that the source of the radioactive decay powering the kilonova is not in the dynamical ejecta, but in other sources such as neutrino drive winds or viscous ejecta [126].

VIII. CONSTRAINTS ON BNS MERGER RATES

Having assessed the robustness of r-process nucleosynthesis from BNS mergers, it still remains to be established whether the amount of ejected material in a BNS merger is sufficient to explain the observed amounts of r-process material in the Milky Way. To this end, and following Ref. [30], we present in Fig. 14 the constraints on the rate of BNS mergers and the required amount of ejected material needed per merger. More specifically, assuming the total amount of r-process material in the Galaxy is $M_{\rm r,gal} \approx 19,000\ M_\odot$ and given a certain merger rate—either per year and galaxy equivalent ($\rm yr^{-1}\,gal^{-1}$, bottom horizontal axis) or per year and cubic Gigaparsec ($\rm yr^{-1}\,Gpc^{-1}$, top horizontal axis)—the black line shows the amount of ejected material per merger required to explain the observed abundances. Similarly, the red line has the same meaning, but only takes into account elements with $A \gtrsim 130$, with a total galactic mass of $M_{\rm r,gal} \approx 2,530\ M_\odot$ [30,131]. The blue-shaded horizontal region indicates the range of dynamically ejected material from BNS mergers in quasicircular (QC) orbits and covered by our simulations as reported in Table II[6] the other two shaded horizontal regions report instead the typical abundances coming from the secular ejecta (pink-shaded region) or from the dynamic ejecta relative to mergers of BNSs in eccentric orbits (green-shaded region).

These constraints should be compared with actual measurements of the merger rates as deduced from different experiments and indicated as vertical lines. In particular, we show as the dot-dashed black line the predicted merger rate of GW170817 [1]. In addition we show the observed upper bound on BNS mergers observed in the first LIGO

[6]The `SFHO-M1.45` model has been omitted because it is not representative.

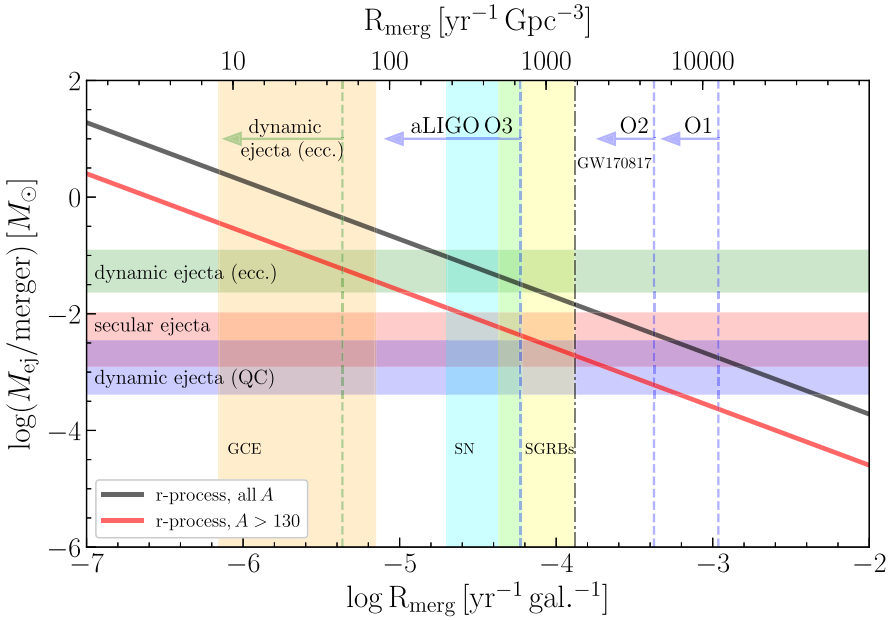

FIG. 14. Ejected material per merger for a given BNS merger rate required to reproduce the observed mass of all (black) and $A > 130$ (red) r-process elements in the Milky Way. The dark blue-shaded regions correspond to the range of values of ejected mass reported in Table II. The red-shaded region corresponds to ejected masses from other sources of ejecta. The dashed vertical gray lines report the observed, O1, and predicted, O2 and O3, upper bounds on BNS mergers from LIGO. The dot-dashed black line is predicted merger rate from GW170817. The orange, light blue, and yellow shaded regions correspond to observational constraints from galactic chemical evolution (GCE), supernova (SN), and short gamma-ray bursts (SGRBs) population synthesis models as defined in the text.

operating run O1, and the predicted upper bounds for the planned future runs O2 and O3 [132]. Additionally, different population-synthesis models are also displayed corresponding to galactic chemical evolution (GCE) [133], supernova (SN) [134], and SGRBS [135].

The red line, horizontal-blue shaded region, and GW170817 overlap in Fig. 14 which indicates that the measured amount of dynamical ejecta, $\sim 10^{-3}\ M_\odot$, from the presented simulations is sufficient to reproduce the observed r-process mass abundances with $A > 130$ in the Milky Way. Associated with GW170817 was a SGRB [8,9] and this confirms that BNS mergers are the central engine of SGRBS and thus the rate constraint predicted by SGRBS [135] is likely indicitative of BNS merger rates. This implies that although we find that there is lower amounts of dynamical ejecta then reported in Newtonian simulations, cf., Sec. V, the frequency of BNSs merger is likely to be sufficiently high to compensate. Furthermore, the geodesic criterion that we employ is a conservative one and only provides a lower bound on the amount of material ejected; by adopting a different criterion, e.g., the Bernoulli one (see discussion in Appendix A), the amount of ejected material can increase up to a factor of 4 for the same simulation.

Another, more exotic scenario of the source r-process, is dynamical ejecta from eccentric BNSs megers. Ejecta masses from these configurations are in fact much larger [24,136], and would be sufficient to explain the observed mass values; however these events are likely very rare and current constraints are not well understood [137].

Finally, it is important to note that our simulations only focus on the dynamical ejecta. There are multiple other channels through which material can be ejected from a merger and they will contribute to the total amount of r-process elements created. For example, simulations of neutrino-driven winds have found similar amounts of ejected material as dynamical ejecta [61]. Likewise, matter ejected from a BH-torus system could be as high as $0.1\ M_\odot$, as estimated semianalytically in Ref. [138]. This suggests that even if the mass ejected from a single channel is alone insufficient to explain the observed r-process masses, the combination of all ejected material from a BNS merger is likely to. In this sense, the blue-shaded horizontal region only represents a lower bound on the total ejected material.

IX. CONCLUSIONS

The simultaneous detection of an electromagnetic counterpart with a gravitational wave from a binary neutron star mergers heralds the beginning of the era of multi-messenger astronomy. Observations now support the picture that material is dynamically ejected from the merger of neutron stars binaries and that such material is neutron-rich and its nucleosynthesis can provide the astrophysical site for the production of heavy elements in the Universe.

Furthermore, this simultaneous detection provides confirmation of the longstanding conjecture that the merger of neutron stars is behind the origin of SGRBs [10–13].

Making use of fully general-relativistic calculations of the inspiral and merger of binary systems of neutron stars, we have investigated the role of initial masses, mass ratio, and EOS on the r-process nucleosynthesis taking place in the dynamical ejecta from BNS mergers. To do so, we have made use of tracer particles that allow us to follow the fluid and that can be used to extrapolate the fluid properties to the late times needed to run nuclear networks codes, together with a simplified neutrino leakage scheme.

Among the several results reported, three deserve special mention. First, we have shown that in the cases considered, the r-process nucleosynthesis from BNS mergers is very robust in that it depends only very weakly on the properties of the binary system, such as the EOS, the total mass or the mass. However, one caveat is that a parameter space exploration depending on the EOS is still rather limited, due to the lack of publicly available fully temperature dependent tables and in future works we intend to explore it more fully with a larger set of EOSs. Overall, while similar conclusions have been reported before, the confirmation coming from our study strengthens the evidence that BNS mergers are the site of production of the r-process elements in the galaxy.

Second, we have employed two different approaches to measure the amount of matter ejected dynamically and found that it is $\lesssim 10^{-3}\ M_\odot$, which is smaller than what usually assumed. There are a number of factors that need to be taken into account when deriving these estimates, namely: the EOS, the neutrino treatment, the criterion for unboundness, the resolution, the numerical methods used. Although these systematic factors can lead to differences as large as one order of magnitude even for the same initial data, we find it unlikely that the mass ejected dynamically can ever reach the values sometimes assumed in the literature of 10^{-2}–$10^{-1}\ M_\odot$. Clearly, a more detailed and comparative study is necessary to better constrain the uncertainties behind the amount of mass lost by these systems.

Third, using a simplified and gray-opacity model we have assessed the observability of the infrared transients associated to the decay of r-process elements, i.e., of the kilonova emission. We have found that all of our binaries show a very similar behavior, peaking around $\sim 1/2$ day in the H-band and rapidly decreasing in luminosity after one day, reaching a maximum magnitude of -13. These rather low luminosities are most probably the direct consequence of the small amounts of ejected matter, thus making the prospects for detecting kilonovae rather limited. Indeed, observations of the kilonova associated with GW170817 suggest higher total ejecta masses [139] but this total also includes other sources such as neutrino driven winds, disk ejecta. Thus a detailed comparison with the new observations will require more sophisticated calculations with improved neutrino treatments to disentangle all the sources of ejecta.

As a final remark we note that even though the r-process abundance pattern does not give us simple clues to the original BNS parameters, e.g., it does not allow us to disentangle various EOS and mass configurations, there are distinguishing features in the ensuing kilonova signal relatable through the difference in ejecta properties obtained in our simulations. In particular, we have found that softer EOSs tend to result in a higher average electron fractions, which implies differences in the type of kilonova produced (blue vs red kilonovae). Additionally, we have found that this difference in electron fraction is highly angular dependent with higher electron fractions around the polar regions and lower along the orbital plane. Even though there is significantly less material ejected along the poles versus the plane, our simulations show that the simplified kilonova modeling, such as that of a homogeneously expanding group of material, need to be adjusted to account for this anisotropic emission. We reserve the investigation of this issue to future studies, where an improved neutrino treatment will be also implemented.

ACKNOWLEDGMENTS

It is a pleasure to thank M. Eichler, M. Hempel, E. Most, A. Perego, and D. Radice for useful discussions. L. B. thanks the attendees of the MICRA 2017 Conference at Michigan State University and of the INT Workshop 17-2b "Electromagnetic Signatures of r-process Nucleosynthesis in Neutron Star Binary Mergers" for useful discussions related to this work. This research is supported in part by the ERC Synergy Grant "BlackHoleCam: Imaging the Event Horizon of Black Holes" (Grant No. 610058), the ERC starting grant "EUROPIUM" (Grant No. 677912), by "NewCompStar", COST Action MP1304, by the LOEWE-Program in the Helmholtz International Center (HIC) for FAIR, by the European Union's Horizon 2020 Research and Innovation Programme (Grant No. 671698) (call FETHPC-1-2014, project ExaHyPE), by the Helmholtz-University Young Investigator Grant No. VH-NG-825, and by the BMBF under Grant No. 05P15RDFN1. L. B. and F. G. are supported by HIC for FAIR and the graduate school HGS-HIRe. The simulations were performed on the SuperMUC cluster at the LRZ in Garching, on the LOEWE cluster in CSC in Frankfurt, on the HazelHen cluster at the HLRS in Stuttgart. Work at LANL was done under the auspices of the National Nuclear Security Administration of the U.S. Department of Energy at Los Alamos National Laboratory under Contract No. DE-AC52-06NA25396. All LANL calculations were performed on LANL Institutional Computing resources. Figures in this manuscript were produced using MATPLOTLIB [140].

APPENDIX A: COMPARISON OF CRITERIA FOR UNBOUND MATERIAL

In Sec. III C, we introduced the criteria by which we determine unbound material. In Secs. IV–V D, we considered only the geodesic criterion for determining unbound material. The justification for this choice of the geodesic criterion is its simplicity and the fact that it provides a lower bound for the total ejected material [99]. An additional benefit of the geodesic criterion is that it does not implicitly depend on the EOS selected, while the Bernoulli criterion, through the enthalpy h, does. This implies that a fluid element, with the same rest-mass density, temperature, and electron fraction, can be unbound or bound depending on the EOS through the Bernoulli criterion. This is a relatively minor trade-off since through the introduction of the enthalpy, the effects of pressure and temperature are taken into account.

Since the specific enthalpy is always grater than one, $h \geq 1$, we have that

$$|hu_t| \geq |u_t|, \tag{A1}$$

and thus the Bernoulli criterion will always result in more material becoming unbound. However, a slight modification of this formula is required. In our simulations, we have an atmosphere that acts as a lower bound for the hydrodynamical quantities. As discussed in Sec. V A we have chosen to evaluate the ejecta at 300 km away from the merger remnant to avoid atmospheric effects. But due to the introduction of the enthalpy, we need to ensure that we are sufficiently above the atmosphere to avoid unphysical atmosphere values entering our calculations. To achieve this, instead of defining unbound elements as satisfying the relation $hu_t \leq -1$, we consider the following modified criterion

$$hu_t \leq (hu_t)|_{\text{atmo}}, \tag{A2}$$

where we evaluate the hu_t at the values set by our atmosphere setup, which is EOS-dependent. For example, for the LS220 EOS this term assumes the value

$$hu_t \leq -1.000163, \tag{A3}$$

instead of -1. Even though this difference is small, the modified constraint does exclude some material from being considered as ejected.

We proceed at comparing the results of the geodesic, the original and the modified Bernoulli criteria in the fiducial case of the `LS220-M1.35` model. In Fig. 15, we show the differences between the three selection criteria in the mass ejection curve. Overall, the behavior for the different criteria is similar, with an ejection phase beginning approximately 2 ms after merger followed by a decrease in the amount of ejected mass. While the geodesic-selected material approaches a constant value, both Bernoulli criteria show a slightly longer increasing phase before settling to a constant. In Table III, we show the comparison of the ejected material for the three criteria and find that by selecting one of the Bernoulli criteria, we obtain approximately 2.5 times as much ejected material when compared to the geodesic one. This increase in the amount of ejecta is similar across all simulations we have performed: the ejected mass is larger by a factor 1.5 to 4 with the Bernoulli criterion as compared with the geodesic one.

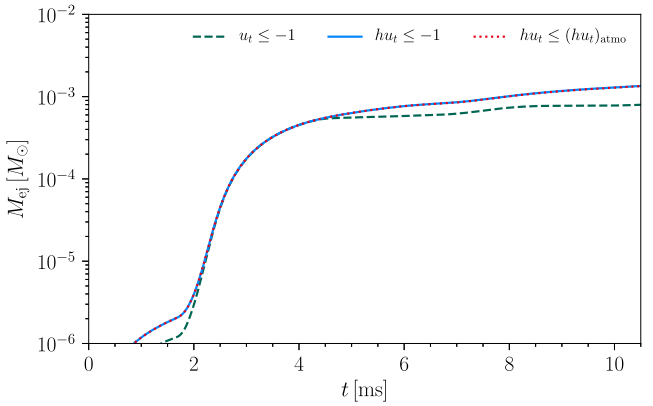

FIG. 15. Mass ejection according to different unboundness criteria for the `LS220-M1.35` model. In green is the geodesic criterion, blue is the original Bernoulli one, and red is the modified Bernoulli thresholded on the atmosphere value. All values have been measured through a detector at 300 km.

In Fig. 16, we plot again the mass distribution in the ejecta of the various quantities relevant for r-process nucleosynthesis, again for the representative `LS220-M1.35` model. Additionally, the average values are summarized in Table III. For the electron fraction and entropy, we do not see drastic changes and the overall structure of the distribution between different criteria. In both cases, there is a slight increase in entropy and Y_e which is to be expected. With both Bernoulli criteria, taking the enthalpy into account includes some thermodynamic effects which will result in more material being ejected due to shock heating. This implies a higher entropy and additionally, more material to undergo neutrino interactions. However, the effects are minimal and the overall nucleosynthesis process will be essentially unaffected.

TABLE III. Average values of the ejected mass, electron fraction, specific entropy and ejecta velocity for different unboundedness criteria in the representative `LS220-M1.35` model.

Criterion	M_{ej} $[10^{-3}\ M_\odot]$	$\langle Y_e \rangle$ -	$\langle s \rangle$ $[k_B]$	$\langle v_{\text{ej}} \rangle$ $[10^{-1}$ c$]$
`geodesic`	0.82	0.10	12.3	2.2
`Bernoulli`	2.09	0.11	13.8	1.5
`modified Bernoulli`	2.07	0.11	13.1	1.5

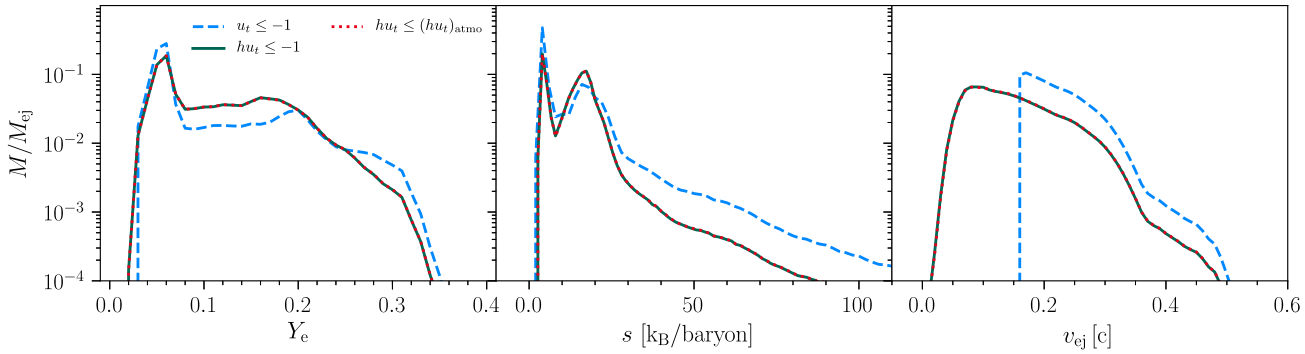

FIG. 16. Comparison of the mass distribution of electron fraction, specific entropy and ejecta velocity in the ejected matter of the representative model LS220-M1.35 for the three unboundedness criteria.

Finally, the most striking difference is in the $v_{\rm ej}$ quantity. In the geodesic criterion, interpreted in its Newtonian limit, a fluid element has to have non-zero velocity at infinity to be considered unbound. This implies a lower cutoff in the velocity distribution, as slowly moving elements, even though able to cross a given detector surface, would not be considered unbound. For both Bernoulli criteria this strict requirement is relaxed by the presence of the enthalpy, which acts as a multiplicative factor larger than one. This means that even slowly moving elements, provided they have sufficiently high enthalpy, would be counted as unbound, and so the velocity distribution acquires a lower end tail and its mean is shifted towards lower values.

APPENDIX B: ADDITIONAL INFORMATION ON EJECTA MORPHOLOGY

In Sec. VII A we analyzed the morphology of the ejected matter, focusing on the angular distribution of the ejected mass and electron fraction. In this Appendix we report the results of the analogous analysis performed on the specific entropy and ejecta velocity distribution.

In the case of the specific entropy, similar observations hold true as for the electron fraction distribution, see Fig. 17: the entropy anticorrelates with the ejected matter. Regions close to the orbital plane tend to have specific entropy values of $10k_{\rm B}$/baryon or lower. This is easily seen in the case of the LS220 EOS simulations.

Around the poles values of the entropy can be very high. These corresponds to the tails shown in Fig. 5, extending to specific entropies of $200k_{\rm B}$ and above. The angular size of the polar high-entropy regions depends on the EOS and mass configuration if each run, but also in this case it appears to (anti-) correlate with the angular distribution of the mass ejection: in cases in which the ejection is strongly focused on the orbital plane, e.g., model LS220-M1.25, higher values of the specific entropy at lower latitudes can be reached, and vice versa.

The tendency of regions with low ejected mass to show higher entropy is easily understood in terms of shock-heating

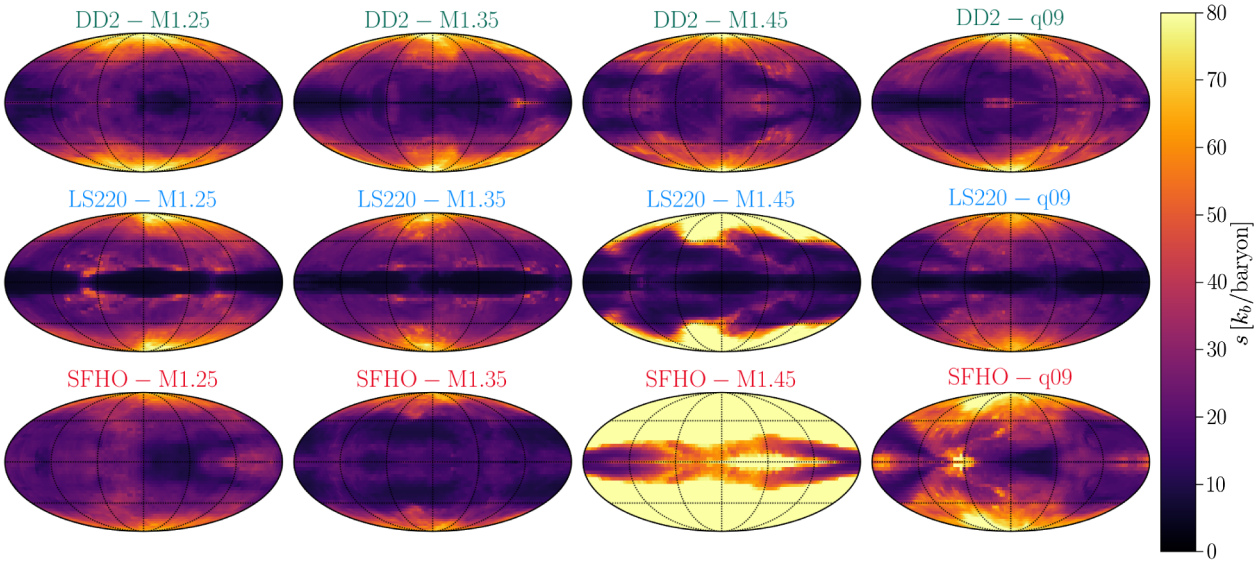

FIG. 17. The same as in Fig. 10 but for the specific entropy averaged over the ejected mass.

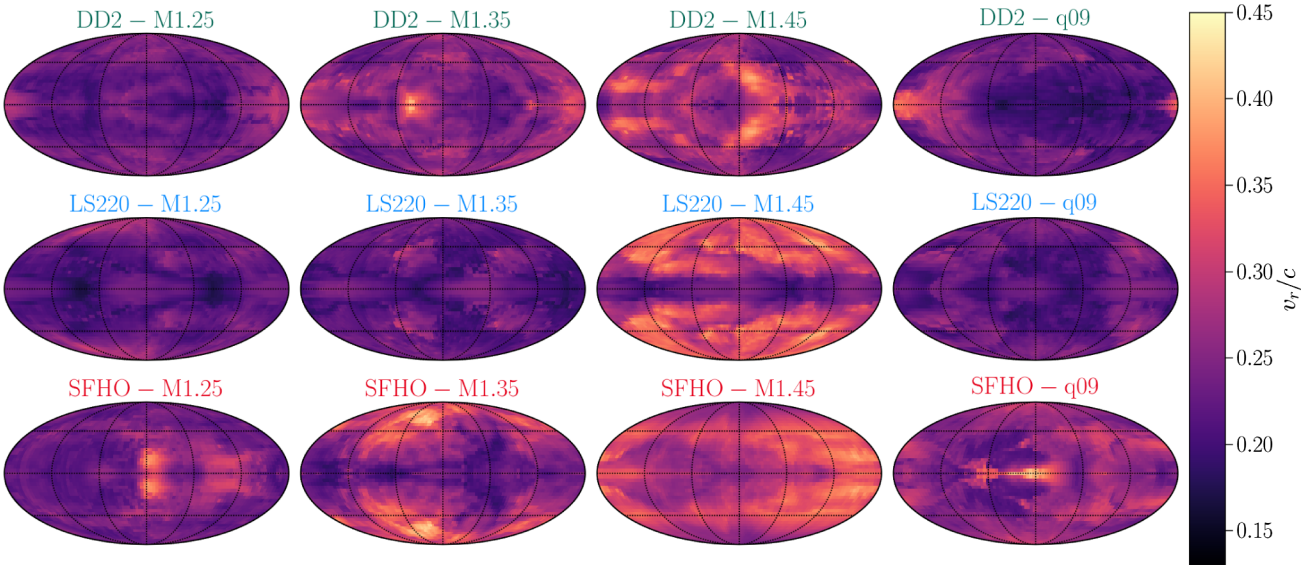

FIG. 18. The same as in Fig. 10 but for the ejecta velocity averaged over the ejected mass.

in rarefied environments: the efficiency of shock-heating is enhanced in low-density media, where less thermal energy is required to heat the material to higher temperatures and raise the entropy. In this sense, the case of the `SFHO-M1.45` model is particularly striking: in this simulation most of the ejected material is at extremely high specific entropy. As observed in the previous discussion, this model also ejects an almost negligible amount of mass, greatly enhancing the shock-heating efficiency.

The velocity distribution, shown in Fig. 18, is instead rather peculiar. For many models, especially the lower mass ones, including the unequal-mass models in the rightmost column of the figure, the material appears to be expanding at the same velocity in most directions, save for a few "hot" or "cold" spots of limited angular size. In the three higher mass models, shown in the third column of Fig. 18, some large-scale structure could be present, but there is no evidence of the correlation observed for the electron fraction or entropy.

Note that, as mentioned in Sec. VII A, the angular distribution of the hydrodynamical and thermodynamical properties of the ejected matter is computed disregarding bound fluid elements [cf., Eq. (10)], i.e., fluid elements that do not satisfy one of the criteria for unboundedness outlined in Sec. III C and Appendix A. In particular, Figs. 10, 11, 17 and 18 have been obtained by considering as unbound fluid elements satisfying the geodesic criterion. If the Bernoulli criterion is employed, the morphology of the ejecta is qualitatively unchanged. This is particularly the case when examining the angular dependence of the ejected mass, electron fraction and specific entropy. The most prominent difference is that the mass ejection extends to higher latitudes, instead of being mostly confined to the orbital plane as in the case of the geodesic criterion. The electron fraction and specific entropy, being anticorrelated with the ejected mass, follow a similar distribution, where however the regions of high Y_e and s close to the poles show a reduced extent. This is to be expected, since the Bernoulli criterion is less restrictive than the geodesic one in defining fluid elements as unbound.

The most striking difference in the ejecta morphology due to the unboundedness criterion is in the distribution of the ejecta velocity. As shown in Appendix A, cf., Fig. 16, the distribution of the ejected mass with respect to its velocity is extends to very low velocity values when the Bernoulli criterion is considered. This is reflected in the angular distribution of the velocity, which for all models where significant mass ejection takes place, has an average value on all angular directions of $\sim 0.15c$, significantly lower than for the geodesic criterion. The Bernoulli-computed distribution of the velocity is also less anisotropic than the geodesic one.

[1] The LIGO Scientific Collaboration and The Virgo Collaboration (LIGO Scientific Collaboration and Virgo Collaboration), Phys. Rev. Lett. **119**, 161101 (2017).
[2] The LIGO Scientific Collaboration and the Virgo Collaboration, Phys. Rev. Lett. **116**, 061102 (2016).
[3] B. P. Abbott, R. Abbott, T. D. Abbott, M. R. Abernathy, F. Acernese, K. Ackley, C. Adams, T. Adams, P. Addesso, R. X. Adhikari *et al.*, Phys. Rev. Lett. **116**, 241103 (2016).
[4] B. P. Abbott, R. Abbott, T. D. Abbott, F. Acernese, K. Ackley, C. Adams, T. Adams, P. Addesso *et al.* (The LIGO Scientific Collaboration, the Virgo Collaboration), Phys. Rev. Lett. **118**, 221101 (2017).
[5] T. Accadia *et al.*, Classical Quantum Gravity **28**, 114002 (2011).
[6] K. Kuroda (LCGT Collaboration), Classical Quantum Gravity **27**, 084004 (2010).
[7] M. Punturo *et al.*, Classical Quantum Gravity **27**, 084007 (2010).
[8] B. P. Abbott, R. Abbott, T. D. Abbott, F. Acernese, K. Ackley, C. aAdams, T. Adams, P. Addesso *et al.* (LIGO Scientific Collaboration and Virgo Collaboration), Astrophys. J. Lett. **848**, L12 (2017).
[9] LIGO Scientific Collaboration and Virgo Collaboration, Astrophys. J. Lett. **848**, L13 (2017).
[10] D. Eichler, M. Livio, T. Piran, and D. N. Schramm, Nature (London) **340**, 126 (1989).
[11] R. Narayan, B. Paczynski, and T. Piran, Astrophys. J. Lett. **395**, L83 (1992).
[12] L. Rezzolla, B. Giacomazzo, L. Baiotti, J. Granot, C. Kouveliotou, and M. A. Aloy, Astrophys. J. Lett. **732**, L6 (2011).
[13] E. Berger, Annu. Rev. Astron. Astrophys. **52**, 43 (2014).
[14] L. Baiotti and L. Rezzolla, Rep. Prog. Phys. **80**, 096901 (2017).
[15] V. Paschalidis, Classical Quantum Gravity **34**, 084002 (2017).
[16] L.-X. Li and B. Paczyński, Astrophys. J. **507**, L59 (1998).
[17] S. Rosswog, T. Piran, and E. Nakar, Mon. Not. R. Astron. Soc. **430**, 2585 (2013).
[18] T. Piran, E. Nakar, and S. Rosswog, Mon. Not. R. Astron. Soc. **430**, 2121 (2013).
[19] D. Grossman, O. Korobkin, S. Rosswog, and T. Piran, Mon. Not. R. Astron. Soc. **439**, 757 (2014).
[20] A. Perego, S. Rosswog, R. M. Cabezón, O. Korobkin, R. Käppeli, A. Arcones, and M. Liebendörfer, Mon. Not. R. Astron. Soc. **443**, 3134 (2014).
[21] S. Wanajo, Y. Sekiguchi, N. Nishimura, K. Kiuchi, K. Kyutoku, and M. Shibata, Astrophys. J. **789**, L39 (2014).
[22] O. Just, A. Bauswein, R. A. Pulpillo, S. Goriely, and H.-T. Janka, Mon. Not. R. Astron. Soc. **448**, 541 (2015).
[23] Y. Sekiguchi, K. Kiuchi, K. Kyutoku, and M. Shibata, Phys. Rev. D **91**, 064059 (2015).
[24] D. Radice, F. Galeazzi, J. Lippuner, L. F. Roberts, C. D. Ott, and L. Rezzolla, Mon. Not. R. Astron. Soc. **460**, 3255 (2016).
[25] O. Just, M. Obergaulinger, H.-T. Janka, A. Bauswein, and N. Schwarz, Astrophys. J. Lett. **816**, L30 (2016).
[26] Y. Sekiguchi, K. Kiuchi, K. Kyutoku, M. Shibata, and K. Taniguchi, Phys. Rev. D **93**, 124046 (2016).
[27] B. D. Metzger and C. Zivancev, Mon. Not. R. Astron. Soc. **461**, 4435 (2016).
[28] M. Tanaka, Adv. Astron. **2016**, 1 (2016).
[29] J. Barnes, D. Kasen, M.-R. Wu, and G. Martínez-Pinedo, Astrophys. J. **829**, 110 (2016).
[30] S. Rosswog, U. Feindt, O. Korobkin, M.-R. Wu, J. Sollerman, A. Goobar, and G. Martinez-Pinedo, Classical Quantum Gravity **34**, 104001 (2017).
[31] R. T. Wollaeger, O. Korobkin, C. J. Fontes, S. K. Rosswog, W. P. Even, C. L. Fryer, J. Sollerman, A. L. Hungerford, D. R. van Rossum, and A. B. Wollaber, arXiv:1705.07084.
[32] B. D. Metzger, Living Rev. Relativity **20**, 3 (2017).
[33] E. Berger, W. Fong, and R. Chornock, Astrophys. J. **774**, L23 (2013).
[34] N. R. Tanvir, A. J. Levan, A. S. Fruchter, J. Hjorth, R. A. Hounsell, K. Wiersema, and R. L. Tunnicliffe, Nature (London) **500**, 547 (2013).
[35] B. Yang, Z.-P. Jin, X. Li, S. Covino, X.-Z. Zheng, K. Hotokezaka, Y.-Z. Fan, T. Piran, and D.-M. Wei, Nat. Commun. **6**, 7323 (2015).
[36] Z.-P. Jin, X. Li, Z. Cano, S. Covino, Y.-Z. Fan, and D.-M. Wei, Astrophys. J. Lett. **811**, L22 (2015).
[37] Z.-P. Jin, K. Hotokezaka, X. Li, M. Tanaka, P. D'Avanzo, Y.-Z. Fan, S. Covino, D.-M. Wei, and T. Piran, Nat. Commun. **7**, 12898 (2016).
[38] E. M. Burbidge, G. R. Burbidge, W. A. Fowler, and F. Hoyle, Rev. Mod. Phys. **29**, 547 (1957).
[39] L. Hüdepohl, B. Müller, H.-T. Janka, A. Marek, and G. G. Raffelt, Phys. Rev. Lett. **104**, 251101 (2010).
[40] L. Hüdepohl, B. Müller, H.-T. Janka, A. Marek, and G. G. Raffelt, Phys. Rev. Lett. **105**, 249901 (2010).
[41] T. Fischer, S. C. Whitehouse, A. Mezzacappa, F.-K. Thielemann, and M. Liebendörfer, Astron. Astrophys. **517**, A80 (2010).
[42] S. Wanajo, Astrophys. J. Lett. **770**, L22 (2013).
[43] C. Winteler, R. Käppeli, A. Perego, A. Arcones, N. Vasset, N. Nishimura, M. Liebendörfer, and F.-K. Thielemann, Astrophys. J. Lett. **750**, L22 (2012).
[44] P. Mösta, S. Richers, C. D. Ott, R. Haas, A. L. Piro, K. Boydstun, E. Abdikamalov, C. Reisswig, and E. Schnetter, Astrophys. J. Lett. **785**, L29 (2014).
[45] N. Nishimura, H. Sawai, T. Takiwaki, S. Yamada, and F.-K. Thielemann, Astrophys. J. Lett. **836**, L21 (2017).
[46] A. P. Ji, A. Frebel, A. Chiti, and J. D. Simon, Nature (London) **531**, 610 (2016).
[47] S. Rosswog, M. Liebendörfer, F.-K. Thielemann, M. B. Davies, W. Benz, and T. Piran, Astron. Astrophys. **341**, 499 (1999).
[48] L. Rezzolla, L. Baiotti, B. Giacomazzo, D. Link, and J. A. Font, Classical Quantum Gravity **27**, 114105 (2010).
[49] L. F. Roberts, D. Kasen, W. H. Lee, and E. Ramirez-Ruiz, Astrophys. J. Lett. **736**, L21 (2011).
[50] K. Kyutoku, K. Ioka, and M. Shibata, Mon. Not. R. Astron. Soc. **437**, L6 (2014).
[51] S. Rosswog, Philos. Trans. R. Soc., A **371**, 20272 (2013).
[52] A. Bauswein, S. Goriely, and H.-T. Janka, Astrophys. J. **773**, 78 (2013).

[53] F. Foucart, M. B. Deaton, M. D. Duez, E. O'Connor, C. D. Ott, R. Haas, L. E. Kidder, H. P. Pfeiffer, M. A. Scheel, and B. Szilagyi, Phys. Rev. D **90**, 024026 (2014).

[54] K. Hotokezaka, K. Kiuchi, K. Kyutoku, H. Okawa, Y.-i. Sekiguchi, M. Shibata, and K. Taniguchi, Phys. Rev. D **87**, 024001 (2013).

[55] L. Lehner, S. L. Liebling, C. Palenzuela, O. L. Caballero, E. O'Connor, M. Anderson, and D. Neilsen, Classical Quantum Gravity **33**, 184002 (2016).

[56] T. Dietrich and M. Ujevic, Classical Quantum Gravity **34**, 105014 (2017).

[57] L. Dessart, C. D. Ott, A. Burrows, S. Rosswog, and E. Livne, Astrophys. J. **690**, 1681 (2009).

[58] D. Martin, A. Perego, A. Arcones, F.-K. Thielemann, O. Korobkin, and S. Rosswog, Astrophys. J. **813**, 2 (2015).

[59] D. Martin, A. Perego, A. Arcones, O. Korobkin, and F.-K. Thielemann, *Proc. Sci.*, NICXIII2015 (2015) 120, [arXiv: 1509.07628].

[60] A. Murguia-Berthier, G. Montes, E. Ramirez-Ruiz, F. De Colle, and W. H. Lee, Astrophys. J. **788**, L8 (2014).

[61] S. Fujibayashi, Y. Sekiguchi, K. Kiuchi, and M. Shibata, Astrophys. J. **846**, 114 (2017).

[62] M. Shibata, Y. Suwa, K. Kiuchi, and K. Ioka, Astrophys. J. **734**, L36 (2011).

[63] K. Kiuchi, K. Kyutoku, and M. Shibata, Phys. Rev. D **86**, 064008 (2012).

[64] D. M. Siegel, R. Ciolfi, and L. Rezzolla, Astrophys. J. **785**, L6 (2014).

[65] L. Rezzolla and P. Kumar, Astrophys. J. **802**, 95 (2015).

[66] R. Ciolfi and D. M. Siegel, Astrophys. J. **798**, L36 (2015).

[67] A. M. Beloborodov, AIP Conf. Proc. **1054**, 51 (2008).

[68] B. D. Metzger, A. L. Piro, and E. Quataert, Mon. Not. R. Astron. Soc. **390**, 781 (2008).

[69] S. Goriely, A. Bauswein, and H.-T. Janka, Astrophys. J. **738**, L32 (2011).

[70] R. Fernández and B. D. Metzger, Mon. Not. R. Astron. Soc. **435**, 502 (2013).

[71] L. Bovard and L. Rezzolla, Classical Quantum Gravity **34**, 215005 (2017).

[72] O. Korobkin, S. Rosswog, A. Arcones, and C. Winteler, Mon. Not. R. Astron. Soc. **426**, 1940 (2012).

[73] S. Typel, G. Röpke, T. Klähn, D. Blaschke, and H. H. Wolter, Phys. Rev. C **81**, 015803 (2010).

[74] J. M. Lattimer and F. D. Swesty, Nucl. Phys. **A535**, 331 (1991).

[75] A. W. Steiner, M. Hempel, and T. Fischer, Astrophys. J. **774**, 17 (2013).

[76] I. Tews, J. M. Lattimer, A. Ohnishi, and E. E. Kolomeitsev, Astrophys. J. **848**, 105 (2017).

[77] Stellarcollapse Website, "Stellarcollapse," https://stellarcollapse.org/.

[78] E. Gourgoulhon, *Lecture Notes in Physics* (Springer Verlag, Berlin, 2012), Vol. 846.

[79] E. Gourgoulhon, P. Grandclément, K. Taniguchi, J. A. Marck, and S. Bonazzola, Phys. Rev. D **63**, 064029 (2001).

[80] L. Rezzolla and O. Zanotti, *Relativistic Hydrodynamics* (Oxford University Press, New York, 2013).

[81] K. A. van Riper and J. M. Lattimer, Astrophys. J. **249**, 270 (1981).

[82] M. Ruffert, H.-T. Janka, and G. Schaefer, Astron. Astrophys. **311**, 532 (1996).

[83] S. Rosswog and M. Liebendörfer, Mon. Not. R. Astron. Soc. **342**, 673 (2003).

[84] F. Galeazzi, W. Kastaun, L. Rezzolla, and J. A. Font, Phys. Rev. D **88**, 064009 (2013).

[85] A. Suresh and H. T. Huynh, J. Comput. Phys. **136**, 83 (1997).

[86] A. Harten, P. D. Lax, and B. van Leer, SIAM Rev. **25**, 35 (1983).

[87] X. Y. Hu, N. A. Adams, and C.-W. Shu, J. Comput. Phys. **242**, 169 (2013).

[88] D. Radice, L. Rezzolla, and F. Galeazzi, Classical Quantum Gravity **31**, 075012 (2014).

[89] M. J. Berger and P. Colella, J. Comput. Phys. **82**, 64 (1989).

[90] D. Radice and L. Rezzolla, Astron. Astrophys. **547**, A26 (2012).

[91] M. Shibata and T. Nakamura, Phys. Rev. D **52**, 5428 (1995).

[92] T. W. Baumgarte and S. L. Shapiro, Phys. Rev. D **59**, 024007 (1998).

[93] D. J. Brown, Phys. Rev. D **79**, 104029 (2009).

[94] T. W. Baumgarte and S. L. Shapiro, *Numerical Relativity: Solving Einstein's Equations on the Computer* (Cambridge University Press, Cambridge, England, 2010).

[95] D. Brown, P. Diener, O. Sarbach, E. Schnetter, and M. Tiglio, Phys. Rev. D **79**, 044023 (2009).

[96] E. Schnetter, S. H. Hawley, and I. Hawke, Classical Quantum Gravity **21**, 1465 (2004).

[97] W. Kastaun, R. Ciolfi, and B. Giacomazzo, Phys. Rev. D **94**, 044060 (2016).

[98] V. Mewes, F. Galeazzi, J. A. Font, P. J. Montero, and N. Stergioulas, Mon. Not. R. Astron. Soc. **461**, 2480 (2016).

[99] W. Kastaun and F. Galeazzi, Phys. Rev. D **91**, 064027 (2015).

[100] T. Rauscher and F.-K. Thielemann, At. Data Nucl. Data Tables **75**, 1 (2000).

[101] P. Möller, J. R. Nix, W. D. Myers, and W. J. Swiatecki, At. Data Nucl. Data Tables **59**, 185 (1995).

[102] P. Möller, B. Pfeiffer, and K.-L. Kratz, Phys. Rev. C **67**, 055802 (2003).

[103] C. Fröhlich, G. Martínez-Pinedo, M. Liebendörfer, F.-K. Thielemann, E. Bravo, W. R. Hix, K. Langanke, and N. T. Zinner, Phys. Rev. Lett. **96**, 142502 (2006).

[104] I. V. Panov, I. Y. Korneev, T. Rauscher, G. Martínez-Pinedo, A. Kelić-Heil, N. T. Zinner, and F.-K. Thielemann, Astron. Astrophys. **513**, A61 (2010).

[105] I. V. Panov, E. Kolbe, B. Pfeiffer, T. Rauscher, K.-L. Kratz, and F.-K. Thielemann, Nucl. Phys. **A747**, 633 (2005).

[106] J. Lippuner and L. F. Roberts, arXiv:1706.06198v1.

[107] S.-i. Fujimoto, N. Nishimura, and M.-a. Hashimoto, Astrophys. J. **680**, 1350 (2008).

[108] F. Timmes and D. Arnett, Astrophys. J. Suppl. Ser. **125**, 277 (1999).

[109] F. X. Timmes and F. D. Swesty, Astrophys. J. Suppl. Ser. **126**, 501 (2000).

[110] C. Freiburghaus, S. Rosswog, and F.-K. Thielemann, Astrophys. J. Lett. **525**, L121 (1999).
[111] B. D. Metzger, G. Martínez-Pinedo, S. Darbha, E. Quataert, A. Arcones, D. Kasen, R. Thomas, P. Nugent, I. V. Panov, and N. T. Zinner, Mon. Not. R. Astron. Soc. **406**, 2650 (2010).
[112] L. Baiotti, T. Damour, B. Giacomazzo, A. Nagar, and L. Rezzolla, Phys. Rev. Lett. **105**, 261101 (2010).
[113] C. Breu and L. Rezzolla, Mon. Not. R. Astron. Soc. **459**, 646 (2016).
[114] M. Hanauske, K. Takami, L. Bovard, L. Rezzolla, J. A. Font, F. Galeazzi, and H. Stöcker, Phys. Rev. D **96**, 043004 (2017).
[115] F. Foucart, R. Haas, M. D. Duez, E. O'Connor, C. D. Ott, L. Roberts, L. E. Kidder, J. Lippuner, H. P. Pfeiffer, and M. A. Scheel, Phys. Rev. D **93**, 044019 (2016).
[116] F. Foucart, M. Chandra, C. F. Gammie, and E. Quataert, Mon. Not. R. Astron. Soc. **456**, 1332 (2016).
[117] F. Foucart, E. O'Connor, L. Roberts, L. E. Kidder, H. P. Pfeiffer, and M. A. Scheel, Phys. Rev. D **94**, 123016 (2016).
[118] T. Dietrich, M. Ujevic, W. Tichy, S. Bernuzzi, and B. Brügmann, Phys. Rev. D **95**, 024029 (2017).
[119] C. Palenzuela, S. L. Liebling, D. Neilsen, L. Lehner, O. L. Caballero, E. O'Connor, and M. Anderson, Phys. Rev. D **92**, 044045 (2015).
[120] S. Rosswog and M. B. Davies, Mon. Not. R. Astron. Soc. **334**, 481 (2002).
[121] J. d. J. Mendoza-Temis, M.-R. Wu, K. Langanke, G. Martínez-Pinedo, A. Bauswein, and H.-T. Janka, Phys. Rev. C **92**, 055805 (2015).
[122] D. M. Siegel and B. D. Metzger, arXiv:1705.05473 [Phys. Rev. Lett. (to be published)].
[123] M. Eichler, A. Arcones, A. Kelic, O. Korobkin, K. Langanke, T. Marketin, G. Martinez-Pinedo, I. Panov, T. Rauscher, S. Rosswog, C. Winteler, N. T. Zinner, and F.-K. Thielemann, Astrophys. J. **808**, 30 (2015).
[124] M. R. Mumpower, R. Surman, D.-L. Fang, M. Beard, P. Möller, T. Kawano, and A. Aprahamian, Phys. Rev. C **92**, 035807 (2015).
[125] D. Martin, A. Arcones, W. Nazarewicz, and E. Olsen, Phys. Rev. Lett. **116**, 121101 (2016).
[126] B. D. Metzger, arXiv:1710.05931.
[127] M. F. Skrutskie *et al.*, Astron. J. **131**, 1163 (2006).
[128] P. Möller, W. D. Myers, H. Sagawa, and S. Yoshida, Phys. Rev. Lett. **108**, 052501 (2012).
[129] J. P. Emerson, W. J. Sutherland, A. M. McPherson, S. C. Craig, G. B. Dalton, and A. K. Ward, The Messenger **117**, 27 (2004).
[130] P. S. Cowperthwaite *et al.*, Astrophys. J. **848**, L17 (2017).
[131] P. J. McMillan, Mon. Not. R. Astron. Soc. **414**, 2446 (2011).
[132] B. P. Abbott, R. Abbott, T. D. Abbott, M. R. Abernathy, F. Acernese, K. Ackley, C. Adams, T. Adams, P. Addesso, R. X. Adhikari *et al.*, Astrophys. J. Lett. **832**, L21 (2016).
[133] B. Côté, K. Belczynski, C. L. Fryer, C. Ritter, A. Paul, B. Wehmeyer, and B. W. O'Shea, Astrophys. J. **836**, 230 (2017).
[134] M. Chruslinska, K. Belczynski, T. Bulik, and W. Gladysz, Acta Astronomica **67**, 37 (2017).
[135] C. E. Petrillo, A. Dietz, and M. Cavaglià, Astrophys. J. **767**, 140 (2013).
[136] L. J. Papenfort, L. Rezzolla, and *et al.* (to be published).
[137] W. H. Lee, E. Ramirez-Ruiz, and G. van de Ven, Astrophys. J. **720**, 953 (2010).
[138] B. Giacomazzo, R. Perna, L. Rezzolla, E. Troja, and D. Lazzati, Astrophys. J. **762**, L18 (2013).
[139] B. P. Abbott, R. Abbott, T. D. Abbott, F. Acernese, K. Ackley, C. Adams, T. Adams, P. Addesso *et al.* (The LIGO Scientific Collaboration, the Virgo Collaboration), arXiv: 1710.05836.
[140] J. D. Hunter, Comput. Sci. Eng. **9**, 90 (2007).